2011

The fall of the Grimsby meteorite—I: Fireball dynamics and orbit from radar, video, and infrasound records

P. Brown

P. J. A. McCausland

M. Fries

E. Silber

W. N. Edwards

See next page for additional authors

Authors

P. Brown, P. J. A. McCausland, M. Fries, E. Silber, W. N. Edwards, D. K. Wong, R. J. Weryk, J. Fries, and Z. Krzeminski

The Meteoritical Society

Meteoritics & Planetary Science 46, Nr 3, 339–363 (2011)
doi: 10.1111/j.1945-5100.2010.01167.x

The fall of the Grimsby meteorite—I: Fireball dynamics and orbit from radar, video, and infrasound records

P. BROWN[1*], P. J. A. McCAUSLAND[1,2], M. FRIES[3], E. SILBER[1], W. N. EDWARDS[4], D. K. WONG[1], R. J. WERYK[1], J. FRIES[5], and Z. KRZEMINSKI[1]

[1]Department of Physics and Astronomy, University of Western Ontario, London, Ontario N6A 3K7, Canada
[2]Department of Earth Sciences, University of Western Ontario, London, Ontario N6A 5B7, Canada
[3]Planetary Science Institute, 1700 E. Fort Lowell Road, Suite 106, Tucson, Arizona 85719, USA
[4]Canadian Hazards Information Service, Natural Resources Canada, 7 Observatory Crescent, Ottawa, Ontario K1A 0Y3, Canada
[5]Air Force Weather Agency/1st Weather Group, Offutt AFB, Nebraska 68113, USA
[*]Corresponding author. E-mail: pbrown@uwo.ca

(Received 27 August 2010; revision accepted 30 November 2010)

Abstract–The Grimsby meteorite (H4–6) fell on September 25, 2009. As of mid-2010, 13 fragments totaling 215 g have been recovered. Records of the accompanying fireball from the Southern Ontario Meteor Network, including six all-sky video cameras, a large format CCD, infrasound and radar records, have been used to characterize the trajectory, speed, orbit, and initial mass of the meteoroid. From the four highest quality all-sky video records, the initial entry velocity was 20.91 ± 0.19 km s^{-1} while the derived radiant has a local azimuth of 309.40° ± 0.19° and entry angle of 55.20° ± 0.13°. Three major fragmentation episodes are identified at 39, 33, and 30 km height, with corresponding uncertainties of approximately 2 km. Evidence for early fragmentation at heights of approximately 70 km is found in radar data; dynamic pressure of this earliest fragmentation is near 0.1 MPa while the main flare at 39 km occurred under ram pressures of 1.5 MPa. The fireball was luminous to at least 19.7 km altitude and the dynamic mass estimate of the largest remaining fragment at this height is approximately several kilograms. The initial mass is constrained to be < 100 kg from infrasound data and ablation modeling, with a most probable mass of 20–50 kg. The preatmospheric orbit is typical of an Apollo asteroid with a likely immediate origin in either the 3:1 or ν_6 resonances.

INTRODUCTION

The detailed connection between classes of meteorites and asteroid types remains a major area of study in planetary science. Linking asteroid spectral families with meteorite classes would enable the large number of spectral observations of asteroids to be fused with the detailed physical information provided by laboratory study of meteorites, making a single narrative describing the formation and evolution of asteroids. Linkages are possible in a number of ways. Spectral matches of asteroids with specific meteorite types have been partially successful, most notably between the HED meteorites and the V-type asteroids (Consolmagno and Drake 1977). However, linkages based on purely spectral affinities are limited by space weathering processes and the differences arising from surface roughness among other complications (cf. Chapman 2004 for a review). Direct spacecraft encounters with asteroids are a powerful method for remote sensing, but necessarily are limited to a few asteroids and may still produce contentious links with specific meteorite classes (e.g., Eros and Ida; Chapman 2004). More promising still are asteroid sample return missions, such as the Hayabusa mission (Yano et al. 2006), which feature both detailed in situ observations of an asteroid, in this case Itokawa (together with similar ground-based observations), coupled with

Table 1. A chronological listing of previous meteorite falls having instrumentally measured orbits. All angular elements are J2000.0.

Name	Date of fall (UT)	Meteorite type	Recovered mass (kg)	V_∞ (km s^{-1})	a	e	i	ω	Ω	Ref.
Příbram	1959/04/07	H5	5.8	20.89	2.4	0.67	10.5	241.8	17.8	1
Lost City	1970/01/04	H5	17	14.2	1.66	0.42	12.0	161.1	283.8	2
Innisfree	1977/02/06	L5	4.58	14.54	1.87	0.47	12.2	177.9	317.5	3
Peekskill	1992/10/09	H6	12.4	14.72	1.49	0.41	4.9	307.6	17.0	4
Tagish Lake	2000/01/18	C2	~10	15.8	1.98	0.55	2.0	224.4	297.9	5
Morávka	2000/05/06	H5	0.633	22.5	1.85	0.47	32.2	203.5	46.3	6
Neuschwanstein	2002/04/06	EL6	6.19	20.95	2.4	0.67	11.4	241.2	16.8	7
Park Forest	2003/03/27	L5	18	19.5	2.53	0.68	3.2	237.5	6.1	8
Villalbeto de la Peña	2004/01/04	L6	3.5	16.9	2.3	0.63	0.0	132.3	283.7	9
Bunburra Rockhole	2007/07/20	Euc	0.324	13.4	0.85	0.25	9.1	209.9	297.6	10
Almahata Sitta (2008 TC_3)	2008/10/07	Ure-Anom	3.95	12.42	1.31	0.31	2.5	234.5	194.1	11
Buzzard Coulee	2008/11/21	H4	> 50	18.0	1.23	0.22	25.5	212.0	238.9	12
Jesenice	2009/04/09	L6	3.6	13.8	1.75	0.43	9.6	190.5	19.2	13

Note: (1) Ceplecha (1977); (2) McCrosky et al. (1971); (3) Halliday et al. (1978); (4) Brown et al. (1994); (5) Hildebrand et al. (2006); (6) Borovička et al. (2003); (7) Spurný et al. (2003); (8) Brown et al. (2004); (9) Trigo-Rodríguez et al. (2006); (10) Bland et al. (2009); (11) Jenniskens et al. (2009); (12) Milley et al. (2010); (13) Spurný et al. (2010).

laboratory studies of returned samples. Asteroid sample return missions offer the best prospect of establishing meteorite–asteroid correspondences.

Another fruitful approach to the asteroid–meteorite connection problem is to make use of the meteorites already impacting Earth and recreate their preimpact orbit. This reverse sample-return approach has now been successful in 13 cases, wherein each meteorite producing fireball event has been instrumentally recorded and a preimpact orbit determined. These previous studies are summarized in Table 1. A variant on this concept is detection of the body prior to impact followed by recovery of meteorites. This was accomplished for the first time for the case of asteroid 2008 TC_3, discovered some 20 h before impact and subsequently shown to be an unusual ureilite based on ground collection of samples. Significantly, substantial ground-based observations of this asteroid were made establishing it as a probable F-class asteroid and thus linking some F-class asteroids and ureilites for the first time (Jenniskens et al. 2009). While this approach is potentially very powerful, the prospect of additional preimpact detections and subsequent meteorite recoveries is not promising as impacts are most likely to occur over oceans, ruling out meteorite recovery, and next generation surveys are most likely to detect small impactors only hours from actual impact and hence not provide useful preimpact orbits or even indication that an impact is impending (cf. Veres et al. 2009). In light of the costs of asteroid sample returns and their scarcity as well as of preimpact detections and follow-on recoveries, determining fireball orbits and recovering meteorites remains a useful diagnostic approach to unraveling asteroid–meteorite linkages.

In this, the first of three articles, we will describe both the fireball and strewn field of an ordinary chondrite (H4–6) meteorite which fell near the town of Grimsby, Ontario, Canada on September 25, 2009 (September 26 0103 UT). Remarkably, the associated fireball occurred near the center of a pre-existing multi-instrument network for meteor observation, the Southern Ontario Meteor Network (SOMN) (Weryk et al. 2007). As a result, the fireball was recorded by seven all-sky video cameras, on three frequencies of a meteor HF radar, by infrasound as well as by numerous local security cameras. Finally, meteorite fragments falling during darkflight were recorded by Doppler weather radars. A second article describes the physical properties, chemistry, mineralogy, and petrology for the 13 recovered fragments totaling 215 g in mass and a third article examines noble gas and short-lived cosmogenic nuclides associated with the cosmic-ray exposure history of the Grimsby fragments.

GENERAL CIRCUMSTANCES OF THE METEORITE FALL

The Grimsby fireball was widely observed over Southern Ontario and the Northern United States on the evening of Friday, September 25, 2009. The event occurred near 9 P.M. local time and as such many people were outside and both heard and saw the fireball. Immediately after the fireball, all seven cameras of the SOMN (Weryk et al. 2007) had data centered around the time of the fireball saved and each was found to have recorded the event under varying conditions. From these initial optical data, a ground solution was obtained suggesting meteorites may have fallen near the town of

Grimsby, Ontario, Canada. A media campaign to alert residents to possible meteorites in the area was launched on October 7, 2009, and as a direct result of this campaign a resident of Grimsby, Yvonne Garchinski, came forward with the first recovered fragment on October 11, 2009 (McCausland et al. 2010). Following this initial recovery, an additional one dozen meteorites have been located through dedicated ground searches and by local residents up to the fall of 2010.

We have organized the article as follows: first we will describe eyewitness reports of the fireball, camera data, multi-frequency backscatter radar signals from the fireball, infrasound recordings of the event, and finally present Doppler radar detection of the falling meteorite debris over Grimsby together with interpretation. We conclude by modeling the final stages of visible flight of the largest fragments, meteorite darkflight, and fireball entry to estimate the mass of initial body, total fall mass and compare our model results to the sizes and locations of recovered meteorites.

Fig. 1. The Grimsby fireball as photographed from downtown Cleveland, OH, by Miranda Nenadovich. The apparent breaks in the trajectory are an artifact of local clouds.

Eyewitness Accounts

At the time of the fireball at 9 P.M. on Friday evening, September 25, 2009, much of the region of Southern Ontario was clear with only patchy cloud in isolated areas. As a result, thousands of people saw the fireball or noticed the flash associated with one of the many flares it exhibited. To place the fireball in context with other past events for which instrumental records do not exist and to help discriminate future fireball events which might produce meteorites, we briefly summarize the visual reports of the event. Eyewitness observations of the Grimsby fireball were reported up to 400 km from the endpoint of the fireball, ranging from as far south as Cleveland, Ohio (USA) (250 km distant), to as far north as Ottawa, Ontario (400 km). By chance, one observer, Miranda Nenadovich, was photographing the skyline of Cleveland at the time of the fireball and recorded the event on her digital camera (Fig. 1). Many eyewitnesses described the fireball as green in color, with several noticeable bright flashes having a bluish-white tint. Eyewitnesses proximal to the endpoint reported several reddish-orange "sparks" invariably described as resembling fireworks that continued to fall after the main light of the fireball had extinguished. Almost all eyewitnesses within a hundred kilometers of the endpoint described the brightest part of the fireball as exceeding the full moon in apparent brightness and several eyewitnesses within 50 km of the fall zone reported the flashes as being " . . . as bright as lightning" or " . . . illuminating the surrounding countryside like daytime." At least one eyewitness noticed the sky turn distinctly blue during the brightest flares. From the eyewitness reports alone, we estimate the fireball absolute magnitude to be ≈ -15 visual magnitude.

Numerous observers reported sounds associated with the fireball. While a handful of these reports made by observers very near or directly under the fireball flight path were delayed sounds consisting of loud booms, distant thunder, or (in the immediate fall zone) loud popping sounds, the majority of sound reports were simultaneous with the appearance of the fireball. These electrophonic sounds (cf. Keay 1992) were variously described as a hissing or like the sound of fireworks falling, popping, or crackling. Almost all observers reporting simultaneous sound were within 30 km of the ground trajectory, with the exception of one witness who heard a distinct hissing sound at the time of the fireball at a distance of 180 km from the endpoint. Given the large amount of instrumental recordings of the fireball, no more detailed analysis of the eyewitness records was undertaken here; a more detailed account of the Grimsby eyewitness data will be given in a later work.

Instrumental Records

All-Sky CCD

The trail of the fireball was recorded by an all-sky CCD system located at the Elginfield Observatory (see Fig. 2 for map and Fig. 3 for the camera image). This system consists of an SBIG ST-1001E camera using a KAF1001E CCD with $1k \times 1k$ resolution and 24 micron pixels. The 16 bit camera uses a Fisheye Peleng

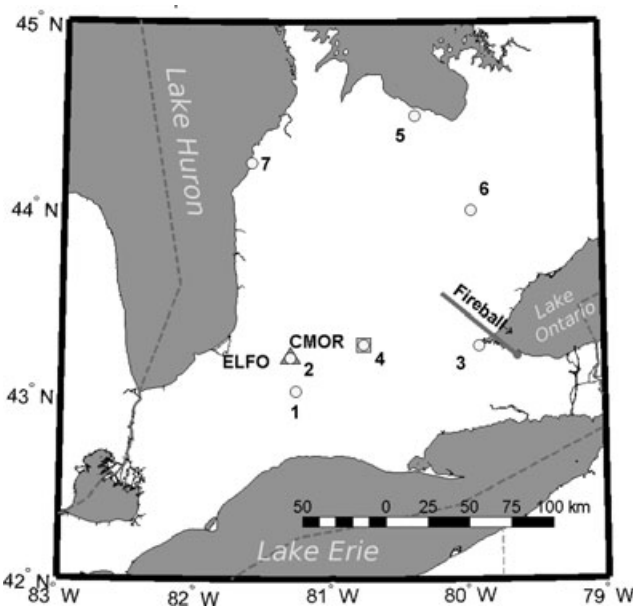

Fig. 2. Map showing distribution of all-sky cameras (yellow) with numbers corresponding to designations given in Table 2, the radar (CMOR) (co-located with camera 4), and infrasound station (ELFO) which detected the Grimsby fireball (ground path shown in red). The all-sky CCD is co-located with camera 2 and ELFO.

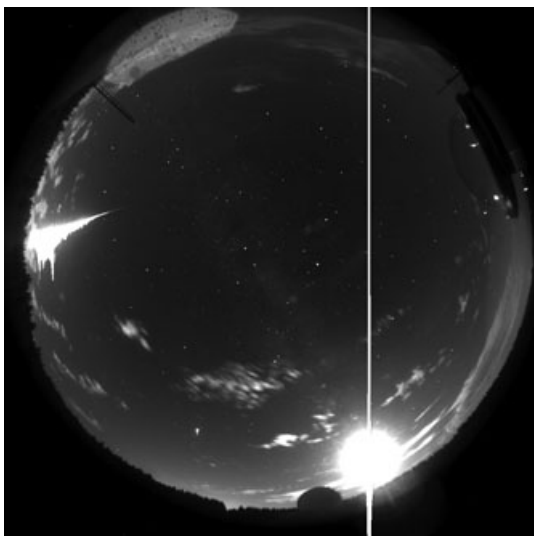

Fig. 3. All-sky CCD fixed image of the Grimsby fireball as recorded at the Elginfield Observatory. The fireball is the bright streak on the left-hand side of the image, while the Moon is the bright circular object at bottom right with vertical bleed lines.

f/3.5 8 mm lens. The fireball was captured on a 60 s exposure and is saturated in the main portion of the trajectory. We attempted to roughly calibrate the lightcurve ignoring bleedover across columns and assuming that the size of the CCD column bleedover is

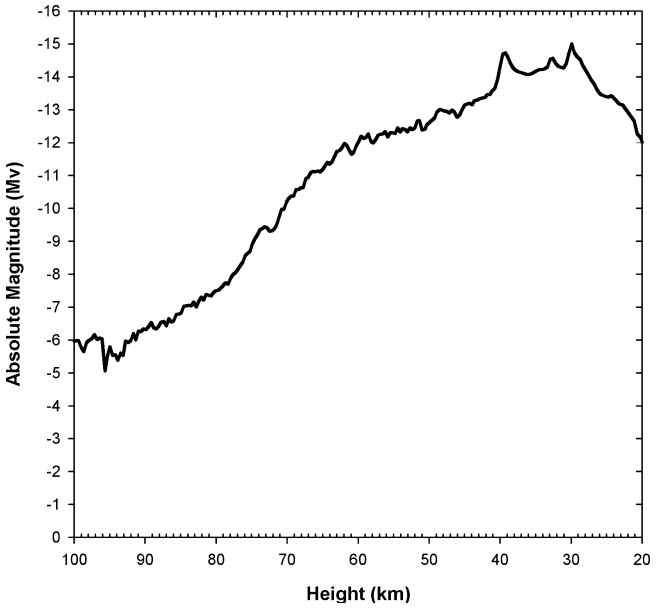

Fig. 4. Approximate lightcurve for the Grimsby fireball from the Elginfield CCD recording. The lightcurve was calibrated using the brightness of Jupiter and assuming the maximum CCD column overflow is proportional to total photon count.

a linear function of brightness, an assumption almost certainly wrong, but one which provides a crude estimate of the shape of the lightcurve and very approximate peak magnitude. The calibration was performed using a range of exposures of Jupiter to find the maximum column overflow as a function of the total photon count. The fireball image was spatially calibrated using the trajectory found using all-sky videos (see next section) and projecting that solution onto the CCD image. Each pixel column was then adjusted for the variation in exposure time associated with the apparent angular velocity of the fireball as constrained by this solution. This permits each CCD column to be associated with a particular height for the fireball. Figure 4 shows the result. Note that the last portion of the trajectory has cloud interference and a greatly compressed pixel scale—the portion of the lightcurve >40 km altitude is the most accurate. The main (first) flare has an estimated absolute magnitude of -14.5 using this technique. We identify the location of the three largest flares with the three CCD columns showing the most saturation. These were then used to roughly establish corresponding heights based on a trajectory solution found using all-sky camera data (see next section). The height of the main flare was found to be approximately 39 km, while the second and third flares occurred at $\sim$33 and $\sim$30 km, respectively, with errors of order 1–2 km resulting from uncertainty as to cross column bleed on the CCD.

Table 2. Grimsby fireball astrometric information based on all-sky video camera data.

Camera #	Range (km)	Height (km)	Q_{max}	Mean res. (m)	σ (m)	Num fields
1	144–133	96–70	86°	194	142	47
2	138–134	94–24	78°	172	118	51
3	105–29	99–20	53°	140	123	98
4	108–92	91–22	72°	105	90	41
5	144–155	86–22	82°	135	140	27
6	113–99	100–79	86°	153	119	38

Note: The range and height show the beginning and final portions of the trajectory visible from each camera; note that positional measurements were not possible between 70 and 25 km height because of saturation effects. Q_{max} refers to the maximum intersection angle between the given camera station and other camera stations. Mean res refers to the average residual between measured points and the best fit trajectory, whereas σ refers to the standard deviation of the measurements relative to the best fit trajectory. The Num fields are the number of useable odd fields for astrometric measurements for each camera.

All-Sky Video Astrometry

The fireball was detected by all seven cameras of the SOMN (Weryk et al. 2007). This camera system has been developed to provide metric data as part of routine coordinated, multi-instrumental observations of bright meteors. These cameras operate at the NTSC frame rate of 29.97 fps, with de-interlaced field data available every 1/60 of second on alternating line pairs within the images. In all that follows, it is the data from odd fields which we have used in measurements; solutions found using the even fields produced identical results within error. The cameras have an all-sky field of view and detection sensitivity for meteors to magnitude −2. All data have been recorded directly to computer disk using an oversampling video card. More details can be found in Brown et al. (2010).

Figure 2 shows the location of the SOMN all-sky cameras together with the ground track of the fireball. The fireball occurred very close to several cameras, most notably camera 3 (Hamilton, Ontario) where the event was in the zenith at its brightest. Despite poorer resolution than photographic camera systems, in this instance the low range and large number of cameras has allowed a fairly precise solution with mean residuals across all cameras averaging approximately 150 m and standard deviations of < 150 m. The details of detection for each camera and the intersection geometry are shown in Table 2.

The positional reductions follow standard procedures; we calibrate each camera's pixel positions using the redsky routine (Borovička et al. 1995). The trajectory was found using the nonlinear least squares approach, assuming a linear trajectory (Borovička 1990). This latter assumption is appropriate given that the full duration of the fireball was found to be approximately 6 s from the closest video station, hence the total curvature (amounting to 180 m vertically across 100 km of pathlength in the worst possible case) is comparable with the precision of the cameras. We found stellar residuals averaging approximately 0.1° in the region of the fireball for both global and local fits using this approach. Typical plate fits used between 50 and 100 stars scattered either over the entire image (global fits) or centered on the region of the images where the fireball occurred (local fits). Solutions using combinations of global and local plate fits were found to produce solutions within their respective formal uncertainty bounds. We also compared solutions using positional measurements from all odd fields, even fields and combined data together and found similar results. Note that camera 7 was not used in any solutions because of heavy local clouds. Camera 1 shows noticeable systematic residuals caused by the fact that the fireball occurs at the extreme edge of the field of view where corrections are most uncertain and no reference stars were available for the fit. Camera 6 also shows a systematic upward trend in horizontal residuals related to asymmetric flaring in the brighter portion of the flight because of dome distortion. However, removing combinations of cameras 1 and 6 still produce trajectory results identical within our uncertainties, so we do not view these small remaining systematic residuals as significant.

Note that because of the brightness of the fireball, camera records between heights of 70–25 km were heavily saturated and were unsuitable for positional reductions. However, because of the sensitivity of the cameras, the fireball was initially detected at 100 km altitude and the end height was just over 19 km, providing significant total trail coverage. The initial velocity was found using the average velocity from four of the seven cameras above 80 km height. Cameras not used for the initial velocity solution included camera 3 (because it had very poor geometry relative to the trail for velocity measurements looking almost directly up the trail), camera 5 where a computer disk issue led to some dropped video frames, and camera 7 where clouds obscured most of the fireball. This uppermost portion of the trail is where no significant deceleration would occur and where the fireball was not yet an extended object, improving astrometric precision. The best fit value for the initial velocity from these best four cameras and associated uncertainty is 20.91 ± 0.19 km s^{-1}.

Table 3. The atmospheric trajectory for the September 26, 2009 Grimsby fireball based on all-sky camera solutions. Geographic coordinates are referenced to the WGS84 geoid.

	Beginning	End
Height (km)	100.5 ± 0.1	19.6 ± 0.1
Velocity (km s^{-1})	20.91 ± 0.19	3.1 ± 1.1
Latitude (N)	43.534° ± 0.001°	43.206° ± 0.002°
Longitude (W)	80.194° ± 0.001°	79.643° ± 0.002°
Slope	55.20° ± 0.13°	
Azimuth of radiant	309.40° ± 0.19°	
Trail length/ duration	94 km/6.04 s	
Time (UT)	01:02:58.40 ± 0.03	01:03:4.44 ± 0.03

Table 4. Heliocentric orbit for the Grimsby meteorite.

α_r	248.93 ± 0.22°
δ_r	55.87 ± 0.11°
V_∞	20.91 ± 0.19 km s^{-1}
V_g	17.89 ± 0.22 km s^{-1}
α_g	242.61 ± 0.26°
δ_g	54.97 ± 0.12°
a	2.04 ± 0.05 AU
e	0.518 ± 0.011
i	28.07 ± 0.28°
ω	159.865 ± 0.43°
Ω	182.9561°
q	0.9817 ± 0.0004 AU
Q	3.09 ± 0.10 AU

Note: (α_r, δ_r) are the right ascension and declination of the apparent radiant (uncorrected for zenithal attraction, diurnal aberration, etc.), V_∞ is the estimated speed at the top of the atmosphere, V_G is the geocentric velocity of the Grimsby meteoroid (i.e., the speed it would have relative to a massless Earth), (α_g, δ_g) are the right ascension and declination of the geocentric radiant (corrected for zenithal attraction, diurnal aberration, etc.), a is the semi-major axis of the orbit, e is the orbital eccentricity, i is the orbital inclination, ω is the argument of perihelion, Ω the longitude of the ascending node, q the perihelion distance, and Q the aphelion distance. All angular coordinates are referenced to J2000.0.

The best fit trajectory solution and orbit from these camera data are given in Tables 3 and 4, while the orbit is graphically depicted in Fig. 5.

All-Sky Video Photometry

Direct measurement of photometry over the entire fireball path with the all-sky video data is not possible because of saturation of the cameras. However, we are able to estimate the early and late stages of the fireball brightness by performing direct aperture photometry of the fireball and compare with the first quarter moon which was approximately 15° above the SW horizon at the time of the event. This was possible for cameras 2, 5, and 6 where the Moon was directly visible and obscured by cloud. All magnitudes are airmass corrected using an extinction coefficient of 0.4.

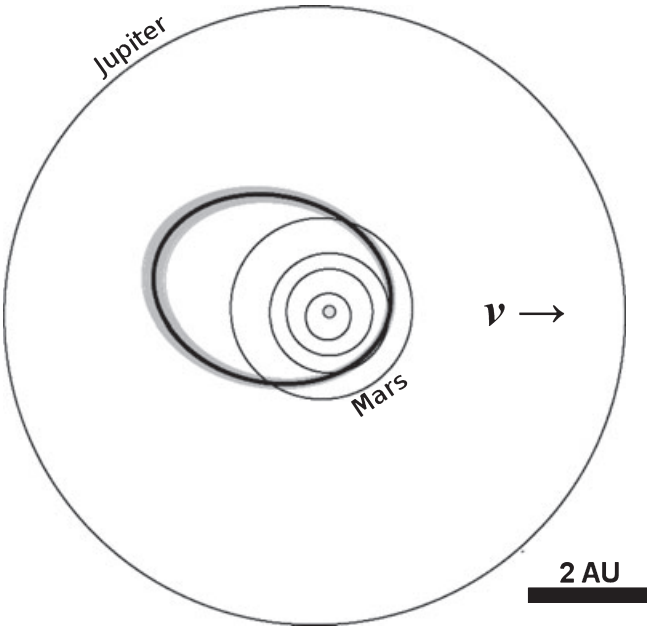

Fig. 5. Orbit for the meteorite-producing Grimsby fireball along with associated error (shown in gray).

For the bright (saturated) portions of the fireball lightcurve, we follow Spurny et al. (2010) who show that the apparent fireball brightness illuminating the sky background can be compared with lunar illumination to yield:

$$M = M_{\text{ref}} - 2.5 \log\left(\frac{B - B_m}{B_m - B_d}\right), \quad (1)$$

where M is the apparent magnitude of the fireball, M_{ref} is the reference magnitude of the Moon (corrected for extinction), B is the average pixel value in a reference region, ideally equidistant from the Moon and fireball, at the time of the fireball, B_m is the average pixel value in the same reference region with the Moon only present, and B_d is the average pixel value in the reference region under a dark (moonfree), clear sky. Cameras 2 and 5 had the Moon suitably visible along with the brightest portions of the fireball to allow this measurement. For each camera, we used a fixed region covering 50 × 50 pixels approximately equidistant from the Moon and brightest portion of the fireball and took the background B_d measurement later the same night (September 26 UT) after the Moon had set and conditions were clear. We emphasize that airmass corrections amounted to 1.5 magnitudes in some cases, with uncertainty in the extinction coefficient (and possible presence of high cloud) introducing at least 0.5 magnitude of uncertainty.

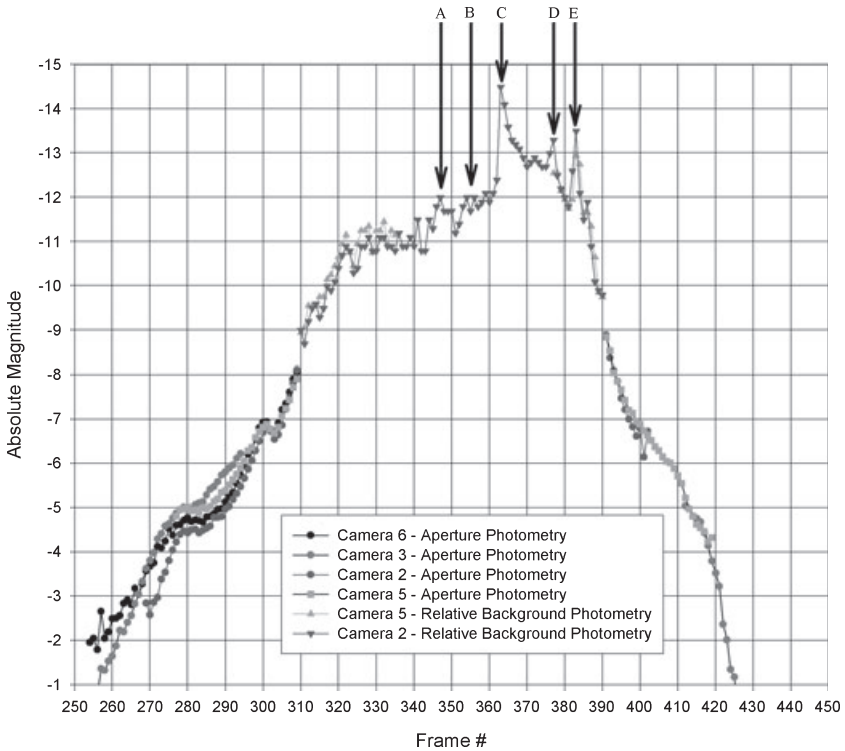

Fig. 6. Grimsby fireball lightcurve combining all available all-sky video camera photometric measurements and techniques—see text for details. The five identified flares are labeled following the convention used in Table 5.

Table 5. Relative burst timings from full frame photometry from all-sky camera records and security camera recordings having frame rates from 10 to 30 fps.

Camera	Burst A	Burst B	Burst C (main burst)	Burst D	Burst E
All-sky	−0.37 ± 0.08	−0.27 ± 0.03	0.00	0.44 ± 0.02	0.22 ± 0.04
Security cameras	−0.52 ± 0.11	−0.24 ± 0.07	0.00	0.39 ± 0.08	0.21 ± 0.04

Finally, to establish the final portion of the fireball lightcurve, we performed direct aperture photometry using camera 3 (where the Moon was not directly visible) and scaled the final portion of the camera 3 lightcurve to match the absolute photometric calibration from camera 5 over the same interval.

The composite lightcurve pieced together using these procedures is shown in Fig. 6. The various cameras show roughly a 0.5 magnitude scatter at the beginning of the trajectory—there is some indication of high cloud present near the Moon for camera 6 so the upward shift of the apparent lightcurve from that station likely reflects an underestimate of lunar extinction—the camera 2 lightcurve is most reliable prior to frame 280. The three cameras show quite similar lightcurve shapes and magnitudes using aperture photometry, providing some confidence in the derived brightness profile. More encouraging still is the agreement near frame 310 and again near frame 390 where the direct aperture photometry is replaced by the relative background photometry. Finally, the independent background brightness measurements from cameras 2 and 5 agree to better than 0.3 magnitudes over much of the saturated portion of the lightcurve, lending further confidence to the final result. From this analysis, the peak brightness in the main flare (burst C) reached −14.8, with two later flares (bursts D and E) of magnitude −13.6 and −13.8, respectively, each with an estimated uncertainty of 0.5 magnitudes. It is clear that fragmentation occurred over most of the flight of the fireball based on the many small maxima present and the deviation of the lightcurve from a classical single-body (nonfragmenting) theoretical lightcurve.

As a check on relative timings of the five most prominent flares, security camera recordings from 10 different cameras located <40 km from the terminal point were examined and full frame (relative) photometry performed. The relative flare timing results

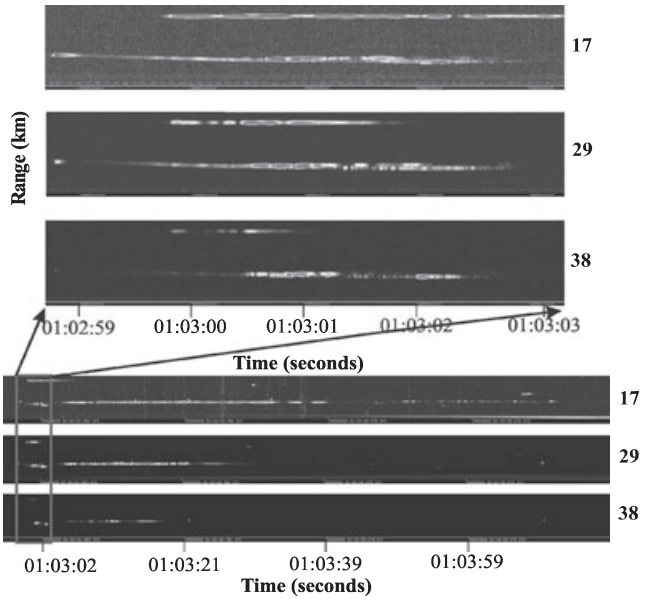

Fig. 7. Radar time–intensity plot showing the Grimsby fireball. The top three plots show the received radar power as a function of range (where the range runs from 15 to 255 km sampled at 3 km intervals) for 17, 29, and 38 MHz data, respectively. The time axis runs from just before 01:02:59 UT on September 26, 2009, to slightly after 01:03:03 UT, each time mark being 1 s on this scale. The lower three plots show a longer time sequence displaying the long enduring body echo at all three frequencies. The time block of the upper plots is shown as the red block in the lower three time series. The total time series at the bottom runs for 70 s, each time mark being separated by approximately 20 s.

from these cameras, in comparison with the all-sky video system results, are shown in Table 5.

Canadian Meteor Orbit Radar Data

The ionization produced by the Grimsby fireball was also recorded on multiple frequencies of the Canadian Meteor Orbit Radar (CMOR). The detailed specifications of the system and general data collection procedures are given elsewhere (cf. Jones et al. 2005; Brown et al. 2008). The radar operates as an interferometer and hence can provide directional information to radar targets in addition to standard range measurement. The procedures used to compute interferometric angles for the system have been presented and reviewed in Jones et al. (1998). The Grimsby fireball was recorded as both a head echo and a long enduring body echo. Figure 7 shows the complete radar record of the fireball while Fig. 8 is an annotated version of the major features visible on that record.

The head echo first became detectable at an altitude of 84 km on the 17.45 MHz radar, 80 km on the 29.85 MHz system, and at 78 km on the 38.15 MHz system. This trend is as expected for head echo detectability as the plasma equivalent radar section decreases as the radar frequency increases (cf. Close et al. 2004; Dyrud et al. 2008). In our case, the scattering physics is likely more complicated than standard theory used for smaller meteors by the presence of multiple fragments and a relatively large scattering cross section, which places most of the head echo signal well into the optical (geometric) scattering regime (cf. Jones et al. 1998). The head echo ended at an altitude of 34 km at 17 MHz and 30 km on the other two frequencies. The higher apparent end height at 17 MHz is an artifact of a stronger contribution from the body echo at high altitude which effectively masked the last (weak) portion of the head echo at this frequency. The height of this nonspecular echo near 70 km suggests either plasma instability processes or may be linked to fragmentation. A remarkable aspect of the fireball geometry relative to CMOR is that the trajectory was positioned such that the specular point (the point along the trail which is at right angles to the radar line of sight) was reached when the fireball was still ablating. This can be seen in Fig. 8 where the reflected radar power from the fireball increases steeply; coincidentally the specular point occurs at a height of 39 km, almost exactly at the position of the main flare detected by the optical systems.

One consequence of this alignment is that the relatively coarse range sampling of the radar (3 km) leads to mixture of the head echo signal and beginnings of the body echo/nonspecular scattering at various points along the trail. Indeed, the total range extent of the head echo (104–88 km) covers only five range sampling bins (each separated by 3 km) total. Despite this coarse range sampling, we can fit each return window to the expected pulse shape (each pulse is 12 km long and is sampled up to four times for strong returns) and are able, in principle, to isolate the pulse location to within 1 km or less for strong signals. To separate the portions of the trail where the head echo dominates over interfering body echo returns, we manually examined the range, interferometry, and estimated heights for a variety of sampling windows at each frequency. By selecting those segments which show the most consistent hyperbolic range–time dependency expected for a head echo moving target, we were able to partially isolate the head echo signal. Using this interferometry and a range fitting routine, we could then measure the instantaneous position of the strongest portions of the head echo at each frequency in three dimensions with an approximate precision of 1 km in range and $< 1^\circ$ in direction. Note that while the absolute interferometry measurements have uncertainties of order one degree, the relative difference between sampled windows shows much greater consistency—this implies that velocities should be measureable with

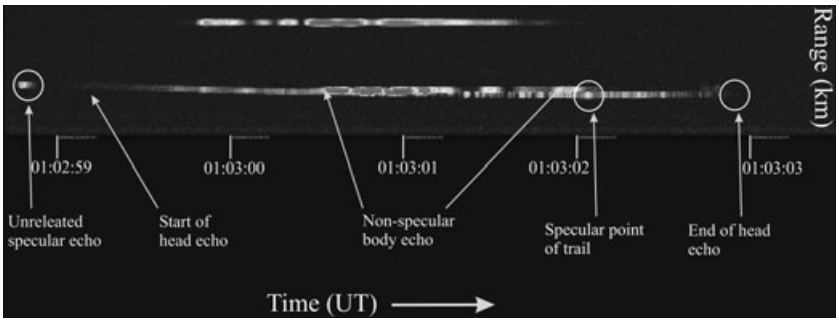

Fig. 8. Details of the radar record of the Grimsby fireball recorded on 29.85 MHz. This range–time–intensity plot samples ranges from 15 to 255 km from the radar (ordinate) 532 times per second (abscissa). The time markers are separated by 1 s and this record begins at 01:02:58.7 UT and ends at 01:03:03.4 UT.

Table 6. CMOR-derived trajectory and speed for the Grimsby fireball based on head echo measurements. The 29.85D and 17.45D (D standing for doppler) rows refer to the overall speed fit for data on the 29.85 and 17.45 MHz system on a pulse-by-pulse basis using a hyperbolic range–time model for the fireball trajectory (see text for details).

Frequency (MHz)	Radiant azimuth (deg E of N)	Radiant altitude (degrees)	Speed (km s^{-1})	Average residual (m)	Number of measurement windows	Height range (km)
17.45	310.1 ± 1.8	55.9 ± 0.9	19.96 ± 0.33	853	38	82–65
29.85	307.1 ± 2.6	56.8 ± 1.4	20.08 ± 0.55	863	25	80–68
38.15	306.5 ± 3.5	58.1 ± 1.8	20.75 ± 0.73	850	22	78–65
17.45D	–	–	19.97 ± 0.02	–	509	82–65
29.85D	–	–	20.02 ± 0.01	–	613	80–68
Camera solution	309.4 ± 0.19°	55.2 ± 0.13°	20.91 ± 0.19	115	–	100–80

higher precision than the trajectory orientation, although the mixture of body echo signals is expected to cause degradation in the solution accuracy.

Taking the earliest portion of the head echo where deceleration should be minimal and performing a simple least squares fit to the 3-D points, a radiant direction and speed for the fireball was determined for each frequency. Table 6 summarizes the results from these radar fits. The resulting radiant for 17.45 MHz data is in good agreement with the camera radiant solution—for 29 and 38 MHz the solutions increasingly differ, likely due to the fewer points useable in the fit for the earliest portions of the trail. This is further reflected in the error in the speeds which increases with frequency as well. Note that the average residuals are much larger than for the camera solution, although this is somewhat misleading as each radar window produces a full 3-D estimate of the fireball position, while the camera residuals refer only to the deviation of the lines of sight from the final best fit linear trajectory. The radar speed estimates refer to a mean speed which extends below the cutoff height used in the camera solutions. These pulse-to-pulse derived range rate–geometry corrected speeds are consistent with each other within their very large error margins.

To better refine the speed from radar data alone, we also attempted to make use of the change in phase received from the head echo on a pulse-to-pulse basis. This technique for measuring head echo speeds using interpulse phase changes is described in detail by Taylor et al. (1996). The basic notion is that the radial change in range for a head echo from one pulse is usually many times the radar wavelength, but if the range rate is approximately known it is possible to infer the number of total phase cycles between pulses and then extract the aliased equivalent phase change. This then allows an independent estimate of the radial velocity at each pulse using only the phase change and measured range. This is equivalent to Doppler velocity estimates on a per pulse basis. As in our case the trajectory orientation is also known, it is possible to compute the true speed at each pulse. As a result of the relatively low signal to noise and the interference from the body echo at some points in the radar record, the uncertainty in the radial velocity measurement on a per pulse basis is quite high, averaging 5–10% of the measured value. In our case the minimum range to the fireball (corresponding to the specular point) is also measured so the radial velocity phase measurements form a time series whose functional form is simply the time derivative of the hyperbolic head echo

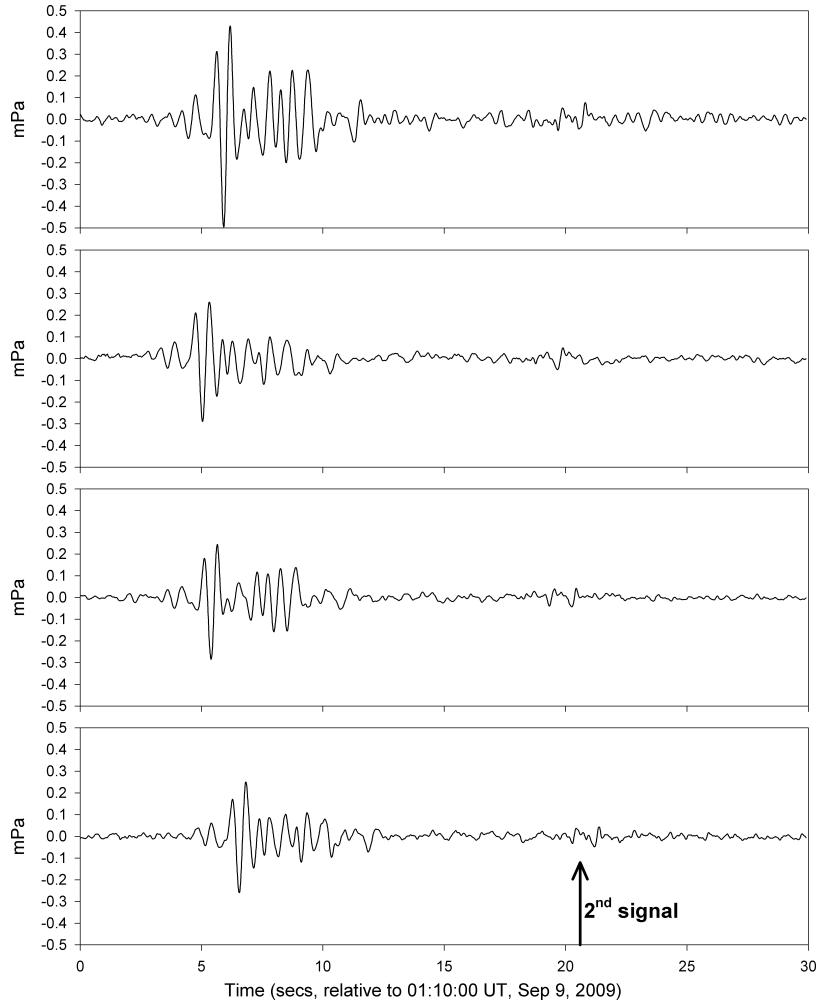

Fig. 9. Infrasound signal from the Grimsby fireball as detected at the ELFO array. The signal has been bandpassed between 0.5 and 5 Hz. The origin time is 01:10:00 UT on September 26, 2009.

range–time function. While we cannot measure deceleration across the head echo signal, we can perform a nonlinear fit to the entire record and get a much more precise average speed measurement as compared with the simple range–interferometry 3-D trail measurement discussed earlier. The results are shown in Table 6—38.15 MHz is omitted as the signal to noise of the head echo is so low, that the individual pulse-to-pulse radial velocity estimates show errors comparable with the aliased velocity increment (2.1 km s^{-1}).

We caution that the error estimates quoted for the interpulse phase speeds are for the errors in fit alone—the true uncertainty is larger. There is also some mixture of body echo signals overlapping the head echo data based on the apparent irregularity in the radial velocity changes notable on both frequencies, even in the cleanest regions of the signal. For this reason, we suspect that the derived speed is not very accurate, although the measurement itself is quite precise, and conclude only that the less accurate radar speed measurements are in broad agreement (within a few percent) of the more accurate camera measurements.

Infrasound Signals

Acoustic signals from the Grimsby fireball were recorded at the Elginfield Infrasound Array (ELFO) at a range of approximately 120 km (see Fig. 2). Infrasound refers to that part of the acoustic frequency spectrum which is in a subaudible (< 20 Hz) frequency range but still above the natural oscillation frequency of the atmosphere normally associated with atmospheric gravity waves (> 0.01 Hz). Its geophysical utility is linked to the fact that at such low frequencies the acoustic energy experiences little attenuation, resulting in sources being detectable over very large distances (cf. ReVelle 1976 for a review of bolide infrasound). Details of ELFO infrasound equipment are given in Brown and Edwards (2009). By beamforming the observed signals

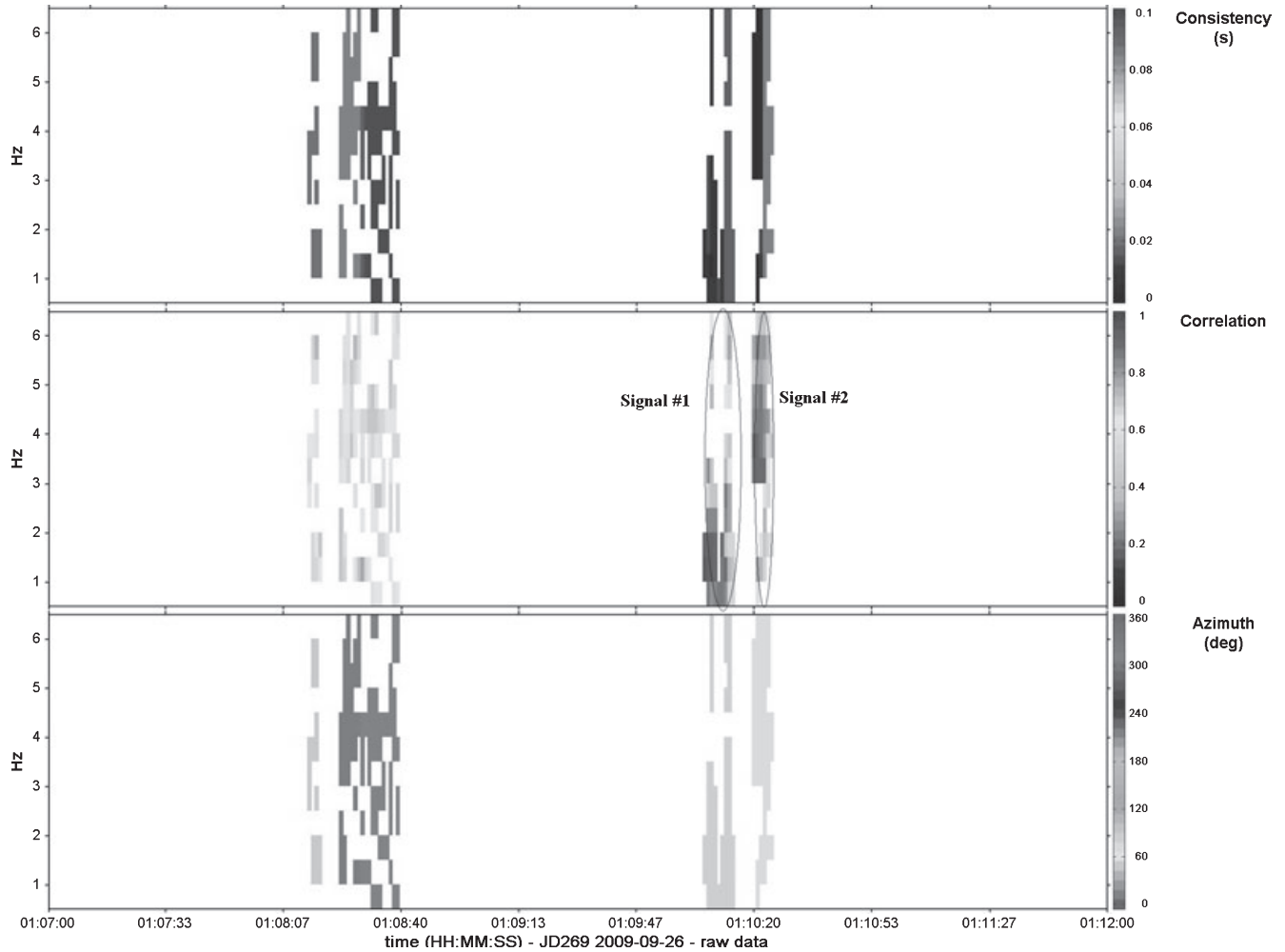

Fig. 10. PMCC family association for ELFO infrasound signal data near the time of the Grimsby fireball airwave arrival. The two distinct signals are marked in the correlation plot—the earlier signal near 01:08 UT is unrelated to the fireball.

and cross-correlating the output from each microbarometer, it is possible to determine the arrival azimuth and elevation for a coherent signal (cf. Evers and Haak 2003). This analysis was performed using the Matseis analysis package (Young et al. 2002).

Figure 9 shows a 30 s time block of the Grimsby fireball pressure–time signal, bandpassed between 0.5 and 5 Hz, from all four ELFO elements. The main arrival begins on element two about 01:10:03 UT. The primary arrival and subsequent wavetrain are followed approximately 15 s later by a smaller, secondary signal.

To better isolate the components of the arrival signal, we make use of the progressive multichannel correlation (PMCC) algorithm (Cansi and Le Pichon 2008). The detection basis of PMCC is a measure of the consistency of delay times (obtained using pairwise cross-correlation) of potential signals across various sub-arrays within the main array. If the consistency falls below a threshold, a detection is declared. Breaking down all these detections in both time windows and a series of frequency bands the PMCC algorithm (cf. Cansi and Le Pichon 2008) then allows identification of aggregates of similar points, with user-defined minimum differences in time, frequency, trace velocity, and arrival azimuth to be grouped together as a single return "family," presumed to be a coherent signal.

Applying this analysis approach to ELFO data, we find two obvious signals identified as "families" shortly after the fireball. The detection is shown in Fig. 10 in correlation, consistency, and azimuth. The two signals identified in Fig. 9 are clearly visible. For the main signal properties (backazimuth, trace velocity, timing, and peak signal frequency) the PMCC and Matseis analysis give almost identical results for the stronger, initial signal—slight differences which remain are attributed to slightly different choices in windowing positions. For the much weaker signal, larger

Table 7. Summary of the infrasound signal associated with the Grimsby fireball as detected at ELFO using a standard bolide infrasound analysis with the Matseis analysis tool (cf. Young et al. 2002) and the PMCC algorithm. Each line shows the signal properties for the first signal (signal #1) and later arrival (signal #2).

Property	Matseis analysis	PMCC
Arrival time (UT)	01:10:04	01:10:04.7
	01:10:19	01:10:19.3
End time (UT)	01:10:12	01:10:10.4
	01:10:22	01:10:22.4
Backazimuth	82.7 ± 1.9	83.1 ± 0.7
(degrees)	76.4 ± 0.1	76.3 ± 0.4
Trace velocity	0.347 ± 0.001	0.352 ± 0.003
(km s^{-1})	0.363 ± 0.001	0.359 ± 0.003
Peak period (zero	0.61 ± 0.01	
crossing method)	1.07 ± 0.13	
(seconds)		
Peak period (PSD	0.76 ± 0.01	
method) (seconds)	0.64 ± 0.53	
Amplitude (Pa)	0.34 ± 0.10	
	0.10 ± 0.02	

Note: PMCC = progressive multichannel correlation.

differences are apparent, a result of the very low signal to noise ratio (SNR) for the second signal.

The two key parameters needed from infrasound measurements to perform fireball energy estimates are signal amplitude and signal period. The amplitudes were computed by simply bandpassing the signal from 0.5 to 5 Hz, consistent with the spectral range of the signal detected by PMCC. The maximum amplitudes were then found using the average backazimuth and trace velocity to identify the delay times to the onset of the signal for each element in the array, and then shifting and phase aligning each element's observed waveform. After phase alignment, the array elements were then stacked to produce an "optimum" waveform, often referred to as the best beam. Once filtered, the waveform's amplitude envelope is computed using the Hilbert transform (Dziewonski and Hales 1972). The peak of the envelope is taken as the maximum amplitude of the signal.

Two approaches were used for estimating the period of each signal arrival. First, a simple zero crossing method was applied to the band-passed waveform. In this technique, the period is measured at the point of maximum amplitude across two cycles and then an average is taken to represent the best estimate for the period. The second approach was to compute the power spectral density (PSD) of the entire signal in a window of sufficient size to contain the signal as determined by the time interval in which the signal backazimuth windows show a consistent value. A series of identically sized windows were then used before and after the event to establish the background PSD. This background was subtracted from the total signal PSD. From this residual PSD, the absolute peak was then taken to be the location of the dominant period with an associated error estimate defined as the interval over which the PSD falls to −10 dB of its peak value. From application of these techniques to numerous bolide infrasound waveforms, we find that the two agree when SNRs are high, but that the PSD approach tends to be more precise, although it rapidly breaks down at low SNRs. Table 7 summarizes the main signal properties from both PMCC (where appropriate) and the standard (Matseis) bolide infrasound signals analysis.

To identify the portion of the fireball trajectory which produced these signals, we used our optical trajectory solution together with the Supracenter (Edwards and Hildebrand 2004) program to ray trace from each measured video point on the fireball to ELFO. The ray tracing direct path solutions provide model estimates of the time delay, expected takeoff angle relative to the fireball path at the source altitude, and arrival angles for signals propagating from the fireball to ELFO. Figure 11 shows the results of this ray tracing model and the observed properties of the signals at ELFO.

The model fits to all observations show a consistent source altitude near 74 ± 2 km for the second (later) arrival. Indeed, the modeled ray deviation from the trajectory heading at this height is almost exactly 90°, indicating that this is in fact the ballistic arrival. The stronger, early arrival shows less source height consistency between timing and backazimuth solutions (generally the two most robust observables) with nominal best fits of approximately 55 and 48 ± 4 km, respectively. As a result of the temperature structure in the lowest few kilometers of the atmosphere, the modeled arrival elevation is most uncertain (as denoted by the large changes in apparent arrival angle over short height intervals below 60 km) with multiple possible solutions near 46, 57, and 68 km. A part of this issue may be the extended duration of the first signal—here we have used the first arrival timing, but the main peak of the impulse occurs 3–5 s later. Using the peak amplitude for arrival timing would push the model delay timing height fits as low as 53 km. Based on these comparisons, the most probable source height for the main arrival appears to be in the interval from 45 to 55 km. At this height the modeled rays make an angle of 110–112° with the fireball trajectory, still within the quasi-ballistic regime previously identified from other meteor-produced infrasound (cf. Edwards et al. 2006). However, note that these ray deviations are the modeled take-off angle for those rays which leave the source and ultimately are predicted to reach the receiver—as such

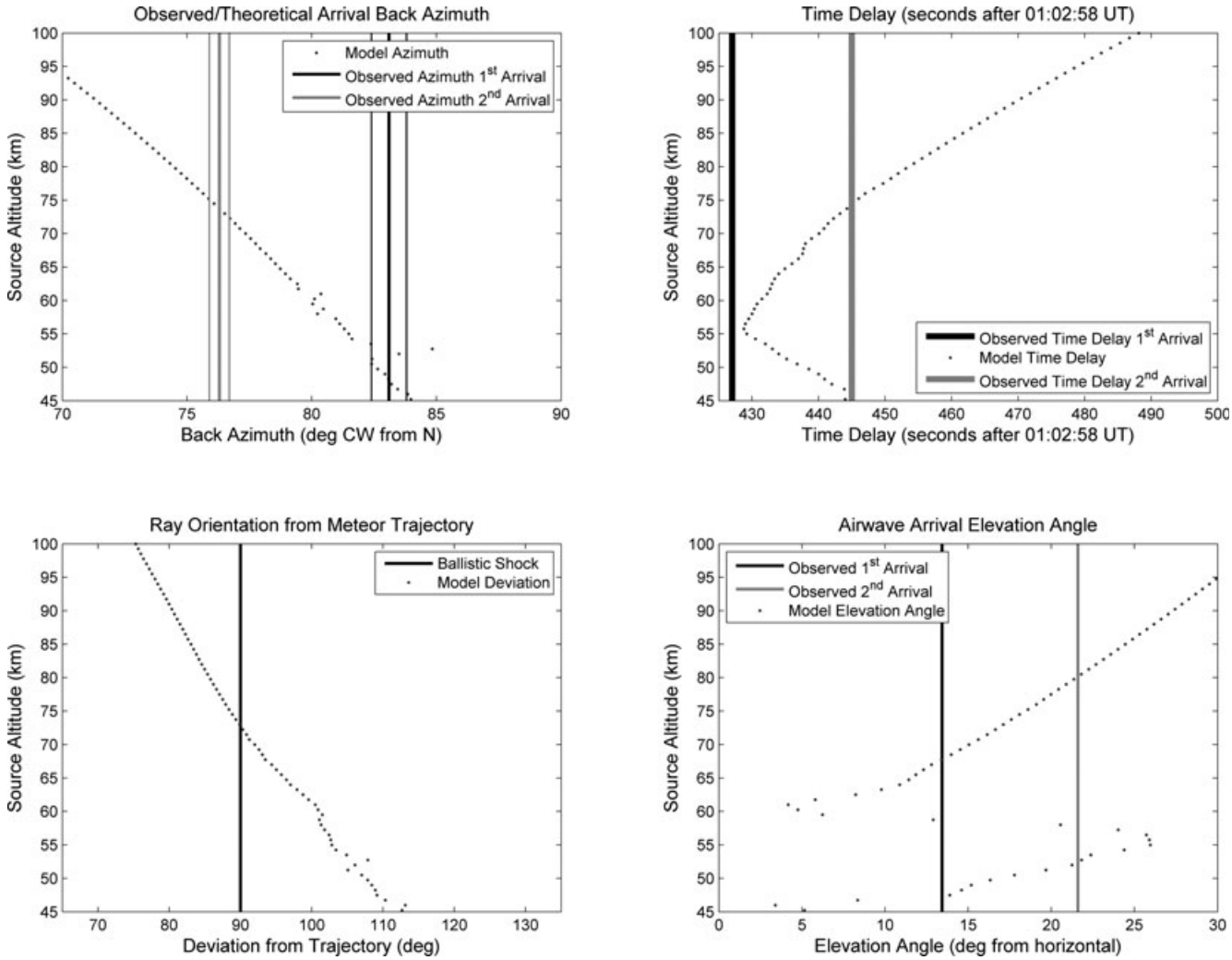

Fig. 11. Ray tracing solutions for the Grimsby fireball. The Supracenter model results as a function of height along the fireball path are shown by the circles in all cases. The observed backazimuth and error for each signal wavetrain are shown by the vertical lines in the upper left plot.

they depend on the details of the atmosphere model used. The purely geometrical solutions show consistent ray deviations 10 degrees lower than the model. This first, strong arrival is plausibly related to the onset of severe fragmentation and perhaps the major fragmentation episode near 40 km height.

To estimate the initial mass/energy for the Grimsby fireball from infrasound signals at short ranges, we compute the theoretical period and overpressure at the ground as a function of mass for our measured source heights. The detailed procedure for this formalism is given by ReVelle (1974). The current implementation incorporates effects due to winds, a complete nonisothermal atmosphere (based on the UKMO model atmosphere for the date and location of the Grimsby fireball; cf. Swinbank and O'Neill 1994) and, based on earlier results (cf. Edwards et al. 2007), assumes that weak shock propagation is valid to ground level.

As the first (strong) signal return is likely associated with the onset of fragmentation (which begins near 47 km in the optical record) the weak-shock formalism is not strictly applicable to this waveform. We therefore use the second, weaker ballistic arrival as a means to gauge the initial mass of the Grimsby fireball. The fact that this earlier arrival is also from a height before any significant fragmentation is detectable in the optical or radar records implies the analytic weak-shock approach should be applicable.

Figure 12 shows the result of this modeling. Model runs using the best estimate for the source height (74 km) bracketed by the possible height error are given for overpressure and period measurements. The

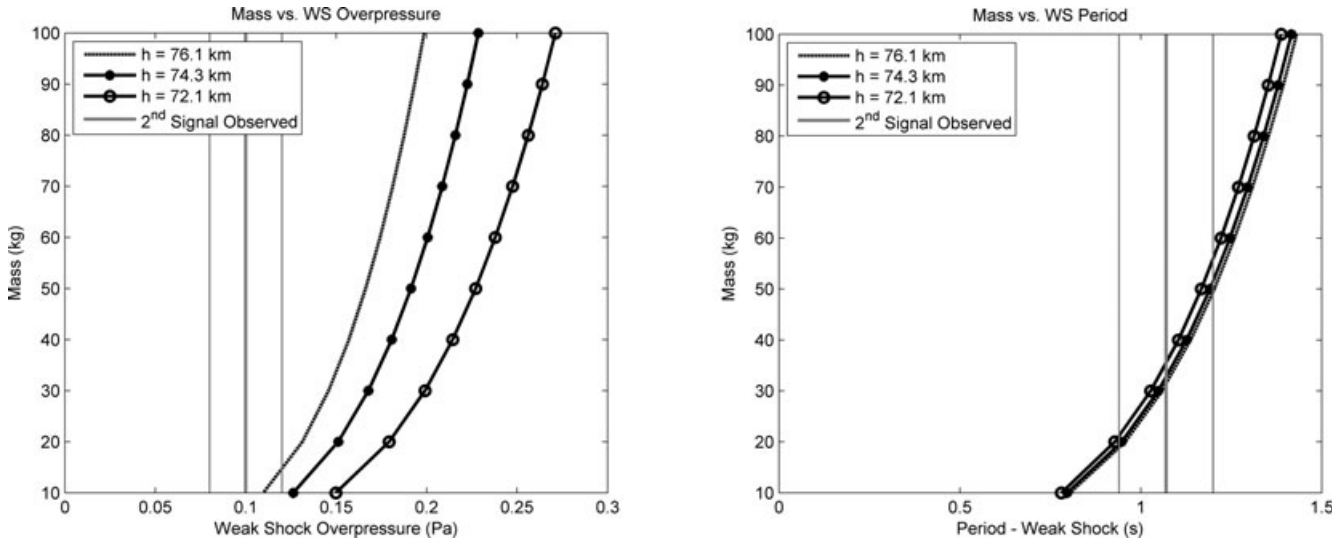

Fig. 12. The predicted overpressure (left) and period (right) for infrasound signals observed at ELFO from the ballistic shock produced by the Grimsby fireball using the weak-shock formalism (ReVelle 1974; Edwards et al. 2007). The expected peak-to-peak amplitude over a range of possible source heights bracketing the estimates from Fig. 10 is shown as a function of mass (black curves) when compared with the observed overpressure value (middle solid vertical line) and observed error range (thinner vertical lines on either side). The right-hand plot shows the model predictions for the period of the waveform at the ground assuming weak-shock propagation occurs to ground level.

overpressure estimates, in particular, are very sensitive to height and also to the assumed damping coefficients used (cf. ReVelle 1974). From past comparisons between meteor photometric masses and infrasonic masses (Edwards et al. 2007), the overpressure model estimates have proven less consistent with source energies computed independently using camera data when compared with period measurements. This may reflect the greater effects of propagation and local site response variations on the signal amplitude (particularly at low SNRs) when compared with the period, a well-known effect in infrasound studies (cf. Christie 2010). Based on this model, the observed overpressure suggests a source mass no greater than approximately 15 kg while the more robust period measurements are consistent with an initial mass of 33 ± 16 kg; hence within error $m_{\text{initial}} < 50$ kg. Interestingly, if we presume our angular deviation derived from the ray tracing modeling is wrong and the first arriving signal is in fact the main ballistic arrival, a reanalysis using the same weak-shock model still places the mass within our uncertainty range. Hence our result is robust against errors in misidentification of the ballistic signal, provided our source height estimates are still approximately correct.

Doppler Radar Detection of Meteorite Debris Plume

Shortly after the luminous flight of the fireball ceased, several locations in the Grimsby area showed radar returns from regional meteorological Doppler radars at altitudes from 2.4 to 6.5 km above ground level (AGL) suggestive of falling debris (see Fig. 13). The most significant signals were detected by the next generation weather radar (NEXRAD) operated by the United States National Oceanographic and Atmospheric Administration (NOAA) located in Buffalo, NY (station KBUF) some 80 km ground range from the fireball endpoint. A weaker signal, plausibly related to the falling meteorite debris cloud, was also detected by the King City radar operated by Environment Canada as part of the Canadian weather radar network at a similar distance of 75 km. This latter detection, however, is more uncertain because of the lower sensitivity and calibration of the Canadian Doppler radar system. In what follows we only analyze KBUF data.

The NEXRAD systems consist of WSR-88D Doppler weather radars operating at a wavelength of 10 cm with peak power of 750 kW and a beam width of approximately 1° to the 3 dB points (cf. Crum and Alberty 1993). At the time of the Grimsby fall, the KBUF radar was operating in clear air mode whereby five elevations angles are scanned over 360° azimuth during a 10 min interval in one degree elevation increments from 0.5° to 4.5°. At the distance from KBUF to the Grimsby endpoint, these scans correspond to heights from 2.4 to 6.5 km AGL. The lowest elevation angles have significant clutter so for our purposes only the scans >1.5° (2.4 km) are used. The radar reflectivity returns represent the relative received

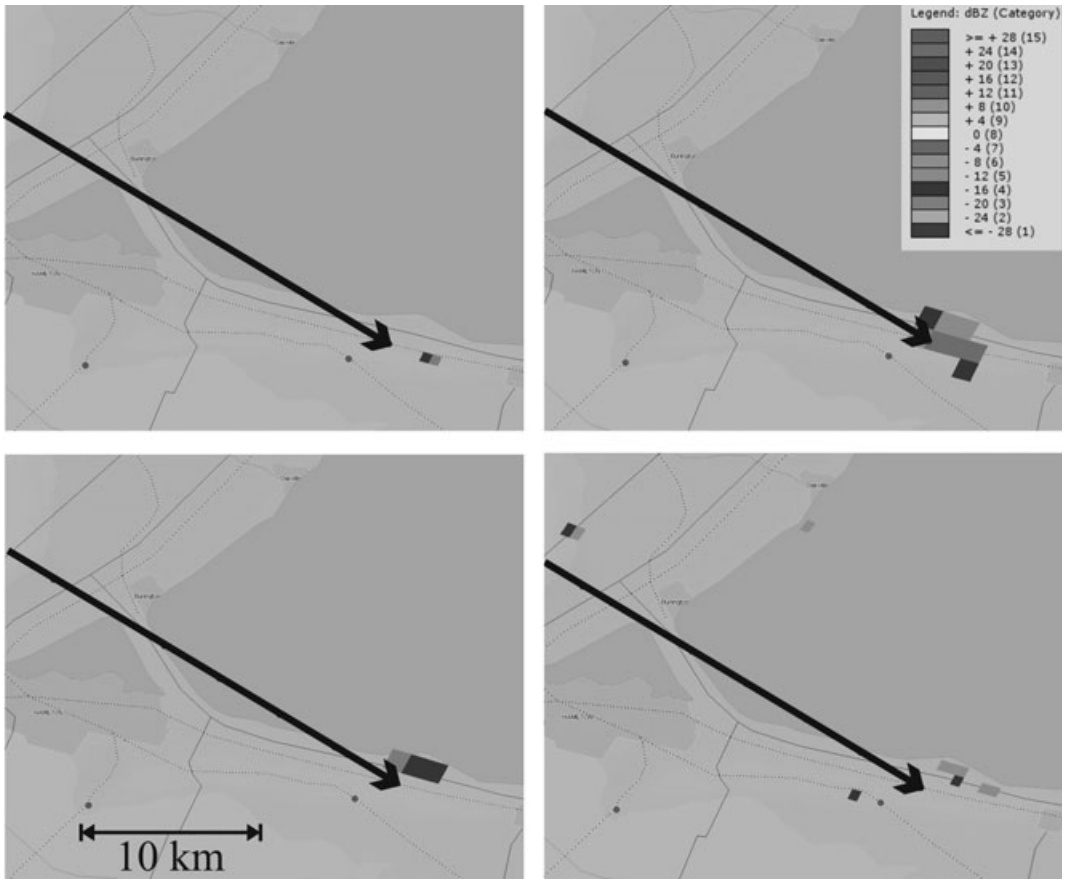

Fig. 13. Doppler weather reflectivity returns from KBUF near the Grimsby fireball endpoint shortly after the fireball. The map shows the video-derived fireball ground trajectory in black—the endpoint (shown by the arrow) is the final luminous point detected by camera 3 at an altitude of 19.7 km. The details of the radar sweep timing and equivalent scanning altitude is given in Table 9. The upper left plot is at $T = 196$ s after the fireball, while the upper right is at $T = 330$ s after the event. The lower left plot is at $T = 422$ s and the lower right at $T = 718$ s postfireball. North is up.

signal returned to the radar in each volume element sampled by the radar at range resolutions of 1 km along the one degree wide beam. The units shown in Fig. 13 (dBZ) are the radar reflectivity factor (Skolnik 2001) used by meteorologists as it permits easy conversion of the returned signal power to a local rain rate; for our purposes we are interested in relative power only. It is unsurprising that NEXRAD is potentially able to detect the falling debris plume from a large fireball as NEXRAD systems have been shown to be capable of detecting birds, insects, smoke/aerosol particles, chaff, and smoke plumes from fireworks detonations (Lemon 1999).

Figure 13 shows a wide area snapshot of the KBUF reflectivity returns from 3 to 12 min after the fireball. In these same elevation cuts, the previous two 10 min sweeps show no returns in this region and the subsequent sweep (starting at 01:20 UT) also shows no signals. The sudden appearance of radar returns immediately under the fireball trajectory is very suggestive of a causal link. The upper atmosphere winds are from the west, so the radar return locations are consistent with falling debris given the known fireball trajectory.

To investigate this link, Fig. 14 shows an enlargement of the region near the fireball endpoint and containing these radar returns. Also shown are the computed locations of individual meteorite fragments released from various altitudes along the trajectory and followed under the action of upper atmospheric winds. In this simulation, we assume each fragment is released with a velocity of 3 km s^{-1} (appropriate to fragments transitioning to darkflight—cf. Ceplecha et al. 1998) and use the methodology outlined in Ceplecha (1987) to model the darkflight. We use the same atmosphere and wind field as described in the analysis of infrasound. At each height, our model iterates the ejected mass until finding a particular mass at which the predicted fall time and height match the observed radar signals. The locations produced from the model do not use the recorded locations of the radar returns. The results of the modeling are summarized in Table 8. Examination

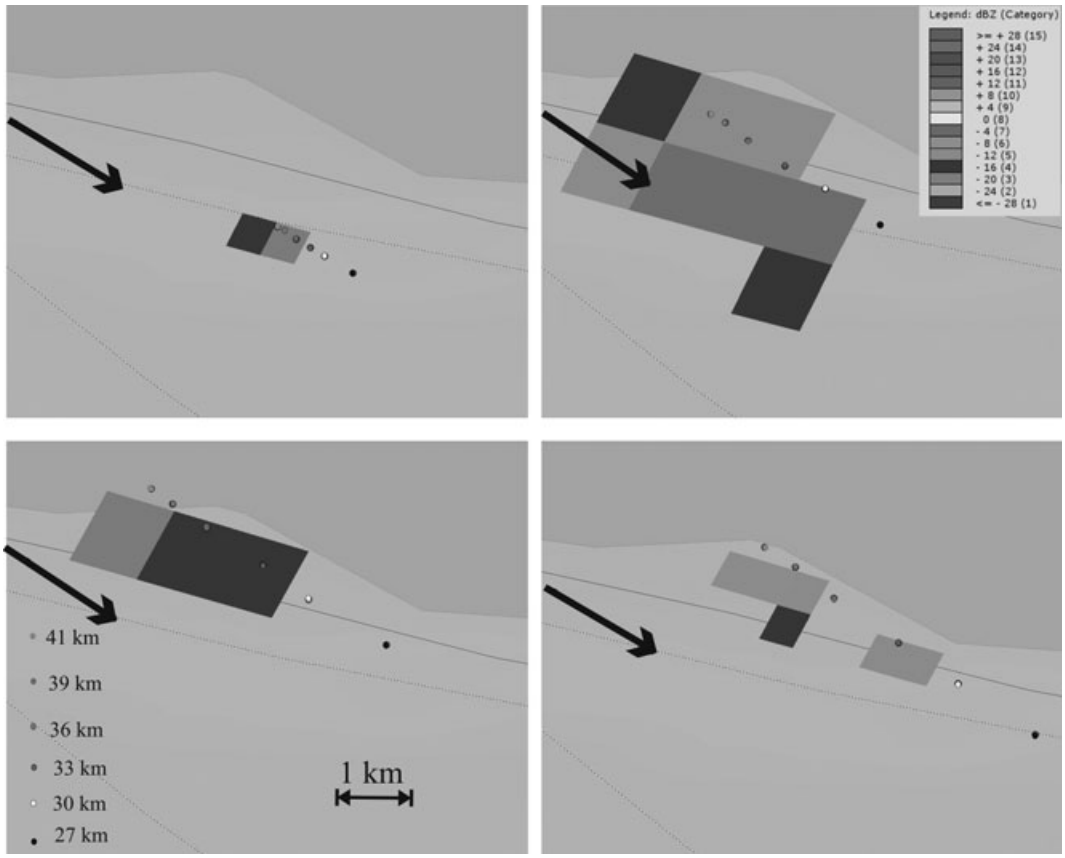

Fig. 14. Doppler weather reflectivity returns from KBUF near the Grimsby fireball endpoint shortly after the fireball. These maps are an enlargement of the immediate fall zone from Fig. 13; the timing is the same as in Fig. 13. The individual colored dots represent a range of darkflight modeled masses released at heights from 27 to 41 km (see legend in lower left box)—the mass ranges are given in Table 8 with the smallest masses always systematically to the east (right).

Table 8. Doppler radar detection summary and comparison with darkflight modeling.

Time (UT)	ΔT (seconds)	Altitude (km)	Mass range (g)	Launch height(s) (km)
01:06:19	196	3.7	520–900	36–42
01:08:33	330	5.2	19–33	30–45
01:10:04	422	6.6	3–6	33–39
01:15:06	718	2.4	1–2	33–39

of the model locations in Fig. 14 shows that they overlap well with the actual radar returns. The "plume" of falling material slowly moves east and north over time as smaller fragments (which take longer to fall) are influenced more by the westward prevailing wind. There is a slight systematic offset in the model predictions compared with the center of the radar returns away from the fireball endpoint; this may be explained as being due to our assumption of spherical fragments—assumption of brick-shaped meteorites was found to produce a shift toward the fireball endpoint and improve agreement. The agreement in spatial locations and the reasonable range in masses predicted from the model (see Table 8) all support the conclusion that this is indeed debris from the fireball recorded by the Doppler radar. It also suggests that the strongest returns are produced by meteorites in the tens of grams range, but that sufficient numbers of >100 g fragments were produced for detectable returns.

It may be possible to constrain the distribution of the number and masses of falling meteorites directly from Doppler radar data but at present this work is immature. We note that probable detection of other meteorite falls using Doppler radar have previously been noted (Fries and Fries 2010). Reflections detected by the NEXRAD software may arise from both direct echoes associated with falling bodies and from beam diffraction because of the atmospheric turbulence arising from the passage of those bodies. Moreover, the magnitude of direct echoes might vary with both meteorite composition to include the amount of fusion crust present. Fundamental measurements of these parameters are presently lacking and this shortfall must be addressed before accurate modeling can be performed of the amount of meteorite mass present in a

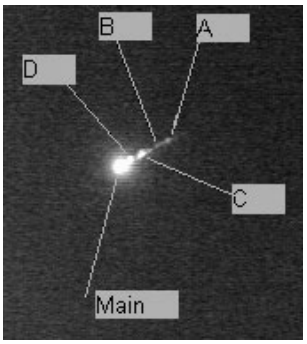

Fig. 15. Single video field showing the Grimsby fireball from camera 3 at a range of 30 km with the leading main fragment at a height of 22.1 km at 01:03:03.24 UT. The five total separate fragments identifiable are spread over a linear distance of 4.7 km at this height.

given NEXRAD reflectivity signal. For this reason, we do not make estimates in this work on the mass distribution based on NEXRAD data, but are hopeful the well-constrained data from Grimsby will allow validation for a future such model.

Fragment Dynamic Mass

Because of its proximity to the fireball endpoint (range $\sim$ 30 km), camera 3 resolved five separate fragments in the final 0.7–1 s of luminous flight. Figure 15 shows an expanded view of one field near the endpoint of the fireball showing these fragments (four trailing the main fragment).

Distinct trajectory solutions for each fragment were found by combining the measurements from camera 3 with data from the other camera stations used in the final best-fit trajectory (Table 3). These fragments became visible as individual objects shortly after the final flare at 29–30 km altitude. The length as a function of time for each fragment was fit assuming constant-deceleration. The quadratic fit was performed iteratively by rejecting points more than 3σ from the best fit solution and reiterating the procedure until all points were closer than this threshold. Deceleration and velocity from this procedure were then evaluated at the middle of the observed arc for each fragment. As the height is also known as a function of time from the solution, we may compute the ratio of the fragment mass-to-area ratio using the standard drag equation (e.g., Halliday et al. 1981):

$$\frac{M_d}{C_d A} = -\left(\frac{\rho_a v^2}{2\dot{v}}\right), \quad (2)$$

where M_d is the dynamic mass, C_d is the dimensionless drag coefficient (here taken to be unity, cf. Carter et al. 2009), A is the frontal cross section area of the fragment, v is the velocity, $\dot{v}$ is the deceleration, ρ_a is the atmospheric mass density at the measurement height.

Table 9 summarizes the flight data for all five fragments, including our estimated deceleration. Measurements were made on both odd and even video fields from camera 3 resulting in one measurement every 0.015 s. The dynamic mass was evaluated at the midpoint of the full video segment where the fragment is visible. In all cases, the fragments continue for another several tenths of a second beyond this point becoming subluminous at velocities of 3–4 km s^{-1}, but measurements become less certain in the final portion of the trail as the fragments become very dim. The large number of measured points and the very small range to camera 3 ($<$30 km) contribute to the unusually good deceleration measurements. The derived masses range from several kilograms for the surviving main mass to just a few grams for the shortest lived fragment (B). Fragment B, in particular, may represent a collection of small fragments as it appears less localized than the other fragments. At least two other fragments (A and D) are potentially in the approximately 100 g range. We caution that variations in shape or drag coefficient beyond our assumed values could easily change these masses by factors of several, so these should only be viewed as representative ranges.

A plot of the lag between the main fragment and each of the secondary fragments near the end of flight produces a nearly linear trend. Making the overly simplistic assumption that each of the secondary pieces is derived from the main fragment and that the linear trend continues from release until the point of observation, an approximate estimate of the height of release for each fragment can be made. This is shown in the last row of Table 9. Fragments C and D have extrapolated release heights fairly near the major fragmentation point at 39–40 km altitude (based on the main flare in the lightcurve and height from the Elginfield CCD). The other two fragment release heights require large extrapolations and the resulting release heights are correspondingly very uncertain—certainly they suggest that fragmentation was a common process across a wide range of altitudes.

METEORITE DARKFLIGHT AND COMPARISON WITH FALL ELLIPSE

Following the initial meteorite find, dedicated searches and local residents recovered an additional dozen fragments before snow ended field searches in early December, 2009. Details of these recoveries and field searches will be presented in a future publication.

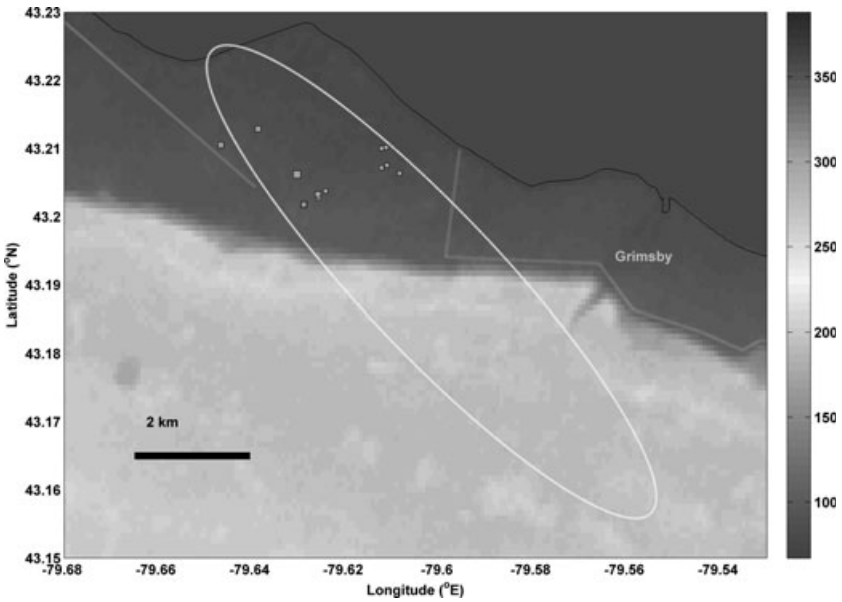

Fig. 16. Find locations for meteorite fragments from the Grimsby fireball. The red line shows the visible fireball trajectory (ending at a height of 19.7 km) while the gray squares are locations of meteorite finds, larger squares representing larger masses.

Table 9. Final fragment dynamic data. Fragment designations follow from Fig. 15. The evaluation height is the height at which the deceleration and velocity are computed from the kinematic fits (see text for more details). The time segment that each fragment was visible is also given. The range of dynamic masses covers plausible variations in shape factor from spherical fragments to hemispherical fragments, but does not include the formal error in the deceleration measurement.

Fragment	Main	A	B	C	D
Evaluation height (km)	21.6	26.4	25.9	24.2	23.4
Deceleration (km s^{-2})	4.4 ± 0.2	5.5 ± 0.5	18.4 ± 5.1	12.7 ± 1.3	12.7 ± 1.1
Velocity (km s^{-1})	4.8	4.2	4.8	4.7	5.0
Dynamic mass range (kilograms)	1.2–4.7	0.026–0.11	0.002–0.007	0.012–0.050	0.025–0.1
Observed end height (km)	19.6	25.7	25.6	23.6	22.7
Segment duration (seconds)	0.67	0.45	0.25	0.45	0.45
Source height (km)	–	70 ± 4	52 ± 5	44 ± 2	41 ± 3

Figure 16 shows the extent of recovered meteorites in the Grimsby area and the ground projection of the fireball path. Figure 17 shows the upper winds at the time of the fireball extracted from a Buffalo, New York, radiosonde release which measured conditions to 32 km altitude just an hour before the event. For heights above 32 km altitude, the UKMO assimilated model profile was used (Swinbank and O'Neill 1994).

The observed fall distribution pattern is consistently to the east of the trajectory. This reflects both the strong crosswinds prevailing from the west and also the paucity of searchable terrain to the immediate south of the fireball path at the eastern fringe of the ellipse because of the Niagara Escarpment.

To check consistency with the fireball trajectory solution and attempt to estimate release altitudes for recovered fragments, we use a model building on the darkflight methodology of Ceplecha (1987) which accounts for atmospheric drag, winds, and Earth's rotation. In the first stage of model runs, individual spherical fragments with masses from 10 kg to 100 mg, in decadal mass intervals, are released at altitudes from 27 to 45 km in 3 km steps. The upper height range corresponds roughly to the observed onset of nearly continuous fragmentation while the lower height is where individually separable fragments become visible (see previous section). In all simulations, fragments are assumed to have velocities of 3 km s^{-1} at the point of release, consistent with other fireball observations indicating that this is the velocity at which luminous flight ceases (cf. Ceplecha et al. 1998). Particularly for larger fragments (>1 kg) we do not expect fragments to reach darkflight condition at higher altitudes, but we include all masses for ease of comparison. The resulting

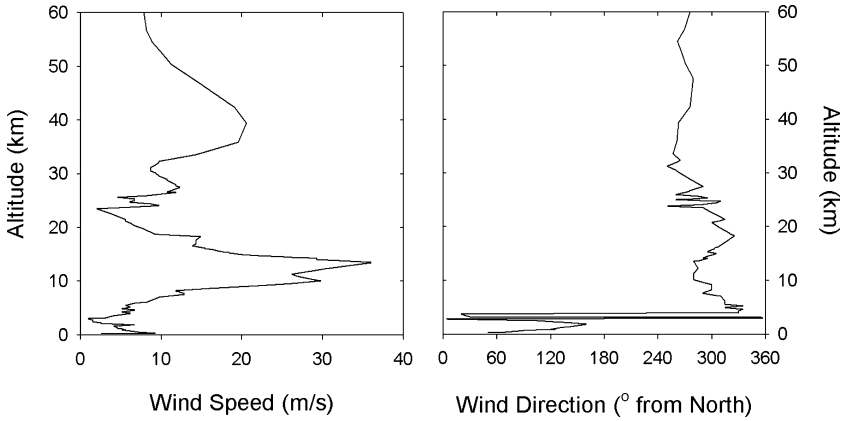

Fig. 17. Upper atmosphere winds at the time of the Grimsby fireball, taken from the Buffalo radiosonde measurement at 0 UT on September 26, 2009 (below 32 km) and UKMO model fit from 32 to 60 km.

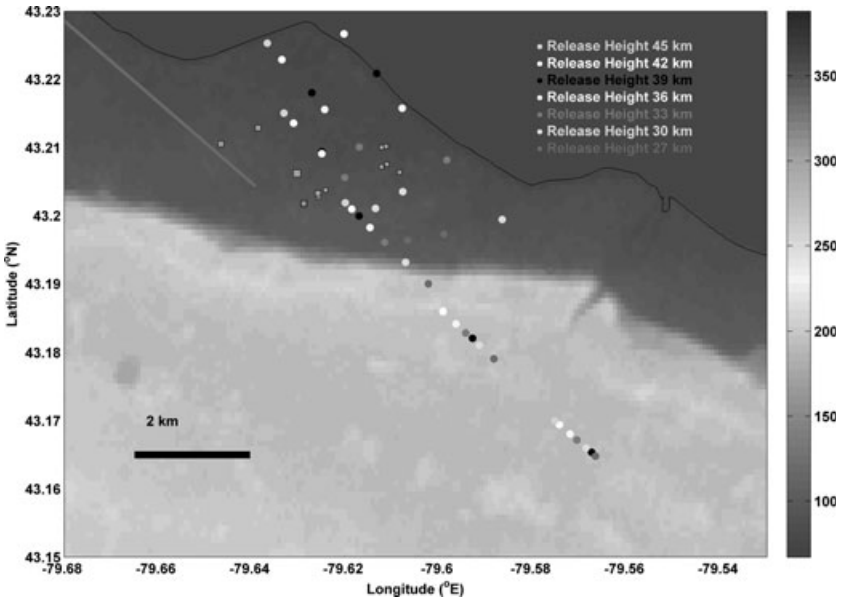

Fig. 18. Darkflight model for the Grimsby fireball (see text for details).

predicted strewn field is oriented along the direction of the trajectory, offset somewhat to the east because of the prevailing westerly winds. In particular masses < 10 g become significantly affected by the WNW jet stream between 10 and 15 km, causing these small particles to be carried to the southeast forming a distinct J-shape (Fig. 18).

In the second stage of the darkflight analysis, we have also computed the expected fall locations for the five individual fragments visible on camera 3 at the end of luminous flight (Fig. 19). Here we use the estimated dynamic mass for each fragment and the actual point along the fireball trajectory where our deceleration fits suggest that the velocity should have been 3 km s^{-1} for consistency with the first stage of modeling.

Finally, we have attempted to gauge the expected ground dispersion resulting from fragment spreads at masses comparable with our recovered masses during luminous flight. In this model, we appeal to the results of Borovička and Kalenda (2003) for the Morávka fireball who measured velocities perpendicular to the main fireball trajectory averaging approximately 50 m s^{-1} (but extending up to 300 m s^{-1}) for individual fragments. We use the same height release points as in the first stage, but now each fragment is given an additional randomly oriented velocity perturbation perpendicular to the main fireball trajectory with a random, normally distributed value having a standard deviation of 50 m s^{-1}. The final result is a footprint region in the fall ellipse for each mass range from each

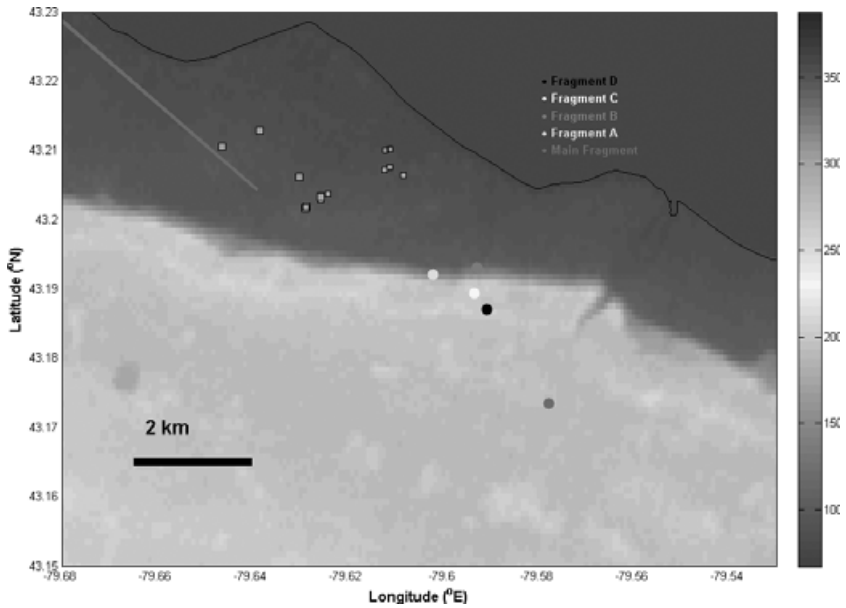

Fig. 19. Darkflight model for the Grimsby fireball for the final five fragments visible from camera 3.

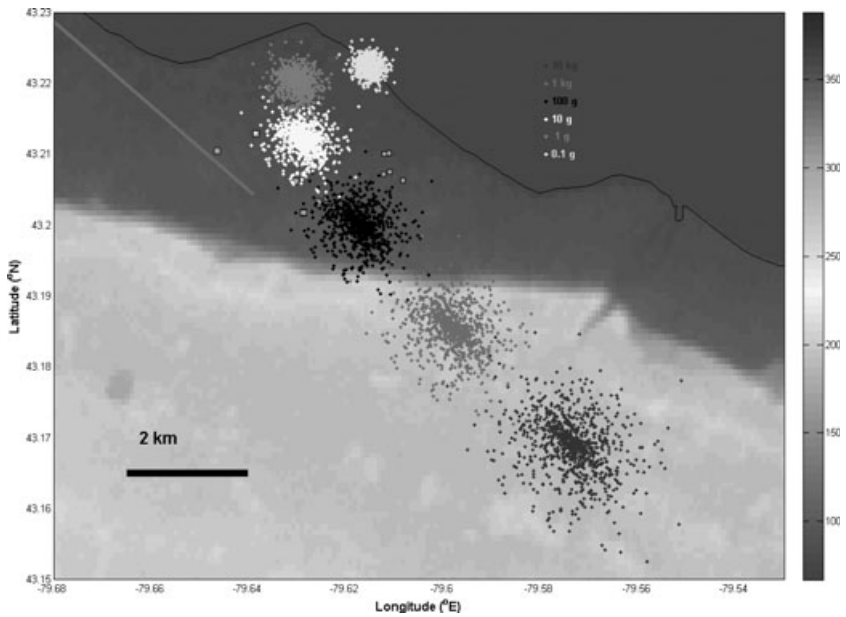

Fig. 20. Darkflight model for the Grimsby fireball showing the expected spread on the ground for masses released at 39 km altitude (main burst) with transverse velocities consistent with those measured for the Morávka fireball.

burst point resulting from plausible variations in the (unknown) perpendicular fragment ejection speed and shape (Fig. 20). The increasing size of the footprint with mass reflects the ability of the atmosphere to decelerate small fragments to terminal velocity very quickly, while larger objects are much more difficult to decelerate and so have a wider footprint.

Comparing the locations of darkflight calculations and observed meteorite recoveries (Fig. 18), it would appear that a large number of smaller finds to the N and E of the main darkflight line are likely from bursts between 30 and 33 km height—the masses of these finds range from 1 to 6 g and are consistent with darkflight predictions assuming these release heights. The larger recoveries lie close to the main modeled darkflight line, up to several hundred meters further to the west of this prediction. In general, these fragments range from 4 to 69 g and are most consistent with darkflight release

> 33 km height. Figure 20 provides an illustration of what the expected transverse velocity during fragmentation might produce on the ground footprint of individual fragments, in this case launched from 39 km altitude, near the main fragmentation point. The spread does not take into account the small additional uncertainty because of positional error in the trajectory/burst location (of order 100 m perpendicular to the path) or of differences in drag because of differing shapes. The mass ranges and probable release altitudes (corresponding to features on the lightcurve) are generally self-consistent. The most discrepant find is a 17 g nearly complete individual found furthest to the west, almost directly under the fireball path. This piece has an unusual waferlike shape, with surface features suggestive of oriented flight indicative of odd drag behavior; it is either from a very high altitude release, perhaps above 45 km, or showed larger drag than the average pieces because of its shape after release from lower (< 45 km) altitudes.

DISCUSSION

Despite extensive searches, no larger pieces along the main darkflight predicted fall track have yet been found. Much of this area is amenable to search and we suggest that relatively few larger fragments (> 100 g) exist. From the deceleration of the largest piece at the endpoint, we do predict that at least one kilogram-sized fragment should have fallen; as shown in Fig. 19, it would be well above the Niagara Escarpment where about 50% of the land is searchable. Lack of any further large pieces suggests that a relatively small total mass reached the ground, consistent with the modest initial mass 33 ± 16 kg predicted from the infrasound record. We note that there is clear evidence for fragments larger than has yet been recovered (69 g) in the dynamic mass estimates of the fragments visible at the end of the fireball luminous flight from camera 3 and also from the Doppler weather data which first showed a signal over Grimsby only 3 min after the fireball, a timing consistent with falling multihundred gram meteorites.

To derive an independent check on this initial mass estimate, we utilize the gross fragmentation model of Ceplecha et al. (1993) in a manner similar to the procedure performed for other meteorite dropping fireballs (e.g., Brown et al. 1996, 2004). The input to this model is the known trajectory, and with the meteorite type (H4–6 chondrite) known we may estimate a shape-density coefficient, K (with $K = \Gamma A \rho^{-0.66}$, where Γ is the assumed drag coefficient, A is the cross sectional area, and ρ is the bulk density in cgs units) of 0.46 (Ceplecha et al. 1998) appropriate for chondritic bodies. To provide a baseline estimate for the ablation coefficient (σ) in the model, we note that the Morávka meteorite fall (Borovička and Kalenda 2003) was an H5–6 with similar entry velocity (22.5 km s^{-1}) to Grimsby and was found to have a mean $\sigma = 0.003$ s^2 km^{-2}; we use this as our starting value. We introduce fragmentation points along the trajectory to attempt to reproduce the gross shape of the lightcurve while simultaneously satisfying the constraints on the velocity. The velocity is known very precisely at the start of the trajectory; from the estimate of the height using the all-sky CCD together with the temporal spacing of the three main flares (C, D, and E) from the all-sky camera recordings full frame photometry we can estimate (with fairly large uncertainty) the velocity of the fireball at these intermediate points. Finally, the last segment of the trajectory has well-determined velocity from the astrometry of the short range camera 3.

Our best fit lightcurve (extracted from Fig. 6) and this velocity profile are compared with a best fit ablation simulation found from forward modeling in Figs. 21 and 22. Our luminous efficiency follows the functional form given by Ceplecha and McCrosky (1976) with calibration using the Lost City meteorite fall by Ceplecha (1996).

We find that to reproduce both the kinematics of the Grimsby fireball and its brightness (simultaneously), we require an initial mass of 27 kg. Our residual mass at the end of luminous flight ($v < 3$ km s^{-1}) is 2.5 kg, consistent with our dynamic mass estimate of the largest (main) fragment detected at the end of the camera 3 record. As an extreme upper mass limit estimate, we may ignore the lightcurve and find the upper mass limit which just barely agrees with the velocity profile within measurement error. We find this to be a mass of approximately 100 kg; we note that at such large initial masses, our nominal estimate for the lightcurve is systematically almost two magnitudes higher than is observed—even given uncertainties in the luminous efficiency in our bandpass, it is difficult to imagine an error in this value of nearly a factor of 10, which would be required to reconcile the lightcurve for such large masses. We conclude from this modeling that the best estimate for the initial mass is 27 kg, with a possible extreme range < 100 kg. These wide boundaries lie within the same (independently derived) initial mass estimates found from the infrasound data/modeling presented earlier.

Interestingly, the initial mass estimates we find from the fireball data are more than an order of magnitude lower than suggested from preliminary noble gas neon ratio estimates (Cartwright et al. 2010) which suggest an initial meteoroid radius > 0.5 m, corresponding to an entry mass > 600 kg for a spherical meteoroid. A similar discrepancy in initial mass estimates between

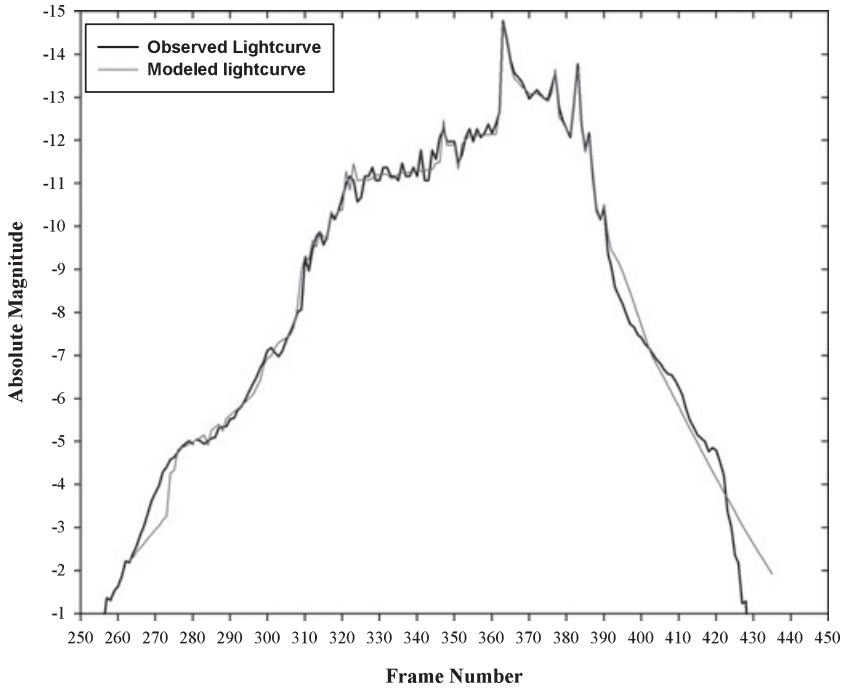

Fig. 21. Model comparison (red line) to measured lightcurve as a function of time (each frame is 1/30 s).

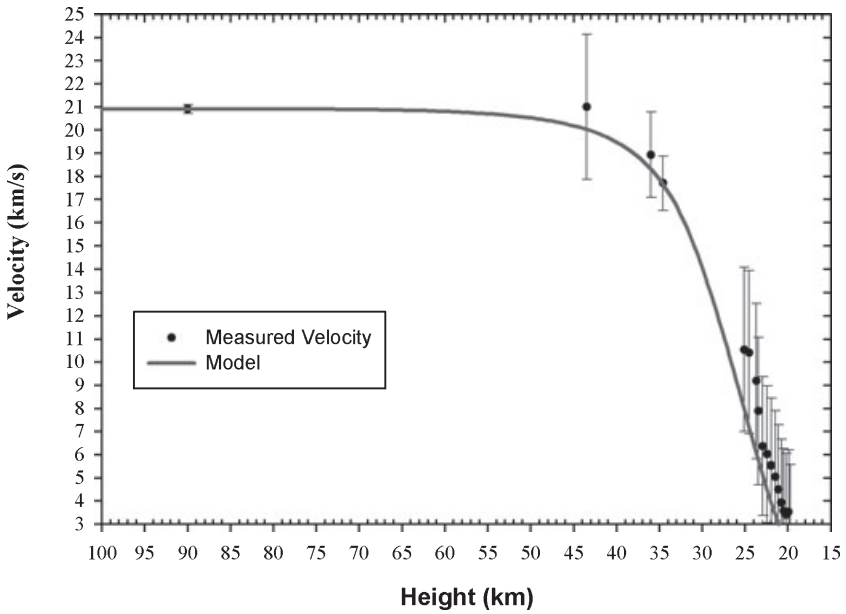

Fig. 22. Comparison of model velocity prediction with observations.

noble gas determinations and flight-derived data was found for the Innisfree fireball (Goswami et al. 1978; ReVelle and Rajan 1979; Wetherill and ReVelle 1981), and Příbram (Ceplecha 1961; Bagnolia 1980). A possible explanation for these differences could be an unusual, nonspherical original meteoroid or multiple exposure history. This discrepancy will be explored further in a later work.

The Grimsby fireball shows signs in its lightcurve and in radar data of fragmentation beginning near 70 km height. From the lightcurve this is based on the difference between our model lightcurve prediction using a nonfragmentation assumption and the observed lightcurve. The deviation between the single body model prediction and observations exceeds two magnitudes beginning near 70 km altitude, with intense

fragmentation starting near 45–50 km height. At these heights, the meteoroid experienced ram pressures between 0.03 and 0.3 MPa, underscoring the intrinsic weakness of the object compared with recovered samples, a result well documented in other cases (e.g., Popova et al. Forthcoming). The major fragmentation near 40 km occurred under 1.5 MPa of ram pressure which is fairly typical for the major fragmentation ram pressure compared with other meteorite-producing fireball events (Popova et al. Forthcoming). Later major fragmentations (bursts D and E) at 33 and 30 km altitude occurred at 3.2 and 3.6 MPa, respectively. Comparison with our numerical ablation model suggests that the earliest bursts (A and B) occurred near 51 and 48 km altitude, respectively.

CONCLUSIONS

The Grimsby meteorite fall is the 14th fall with an instrumentally measured preatmospheric orbit. The orbit is a typical Apollo-type and suggests a Main Belt origin most probably in either the 3:1 or ν_6 resonance (Bottke et al. 2002) from measured a,e,i values. The fireball associated with this H4–6 chondrite reached a peak magnitude of −14 to −15 during a major flare/fragmentation episode at a height of 39 km under 1.5 MPa of ram pressure. The final luminous portion of the trajectory was visible to 19.7 km height. Based on dynamic mass estimates of the leading fragment at this height the main fragment is several kilograms. To date only 215 g of material has been recovered; we crudely estimate a total fall mass on the ground of order approximately 5 kg, mainly in the form of several large (unrecovered) fragments. From the Doppler weather record of the meteorite debris plume and the multiple trails visible in the camera 3 record, at least a handful of fragments larger than the current main mass (69 g) must have fallen.

The fireball initial entry velocity is best constrained to 20.91 ± 0.19 km s^{-1} from all-sky video camera records from four separate stations; independent velocity estimates from radar head echo data are several percent lower than this value, but suffer from trail echo contamination making these values more suspect. The camera-derived radiants are consistent within error of those derived from three separate radar measurements of the head echo trajectory.

An initial mass of 33 ± 16 kg is determined from infrasound modeling of the observed waveform while our ablation simulation predicts a similar best-fit initial mass near 27 kg, with an upper limit < 100 kg. These values are nearly one order of magnitude lower than that predicted on the basis of noble gas measurements from a single fragment (Cartwright et al. 2010).

Due in part to local terrain in the fall ellipse and an understandable focus in recovery efforts near the first recovered fragment, all fragments (which are quite small) have been found in the far uprange (western) portion of the fall zone. From darkflight modeling, we estimate that most of these smaller fragments originate with the fireball detonations in the 30–40 km height range.

Additional field searches for larger fragments of the Grimsby fall would appear warranted based on this analysis.

Acknowledgments—The authors dedicate this article to the memories of Dr. Douglas ReVelle and Dr. Zdenek Ceplecha who individually and collectively laid much of the modern foundation for observational and theoretical interpretation of meteorite-producing fireballs. Use of computer code in our analysis provided by J. Borovička and Z. Ceplecha is gratefully acknowledged.

P. G. B. thanks the Canada Research Chair program, the Natural Sciences and Engineering Research Council of Canada and the NASA Meteoroid Environment Office for funding support. We thank D. Welch (McMaster University), the Toronto Centre of the Royal Astronomical Society of Canada, M. Castel, P. Zelichowski, and A. Oslach for hosting cameras of the Southern Ontario Meteor Network. P. J. A. M. acknowledges support from the Centre for Planetary Science and Exploration, University of Western Ontario. We thank A. Hildebrand for his invaluable assistance in recovery of Grimsby fragments. R. Botting, M. Farmer, Y. Garchinski, T. Garchinski, P. Hermann, and R. Wesel provided recovery data and/or loan of recovered fragments for analysis. Helpful reviews from J. Vaubaillon and O. Popova improved an earlier version of this article.

Editorial Handling—Dr. Donald Brownlee

REFERENCES

Bagnolia C. 1980. Mutiple fall of Příbram meteorites photographed: 12. Pre-atmospheric size of the Příbram meteorite based on studies of fossil cosmic ray tracks and spallation products. *Bulletin of the Astronomical Institute of Czechoslovakia* 31:51–58.

Bland P. A., Spurný P., Towner M. C., Bevan A. W. R., Singleton A. T., Bottke W. F., Greenwood R. C., Chesley S. R., Shrbeny L., Borovička J., Ceplecha Z., McClafferty T. P., Vaughan D., Benedix G. K., Deacon G., Howard K. T., Franchi I. A., and Hough R. M. 2009. An anomalous basaltic meteorite from the innermost main belt. *Science (New York, N.Y.)* 325:1525–1527.

Borovička J. 1990. The comparison of two methods of determining meteor trajectories from photographs. *Bulletin of the Astronomical Institute of Czechoslovakia* 41:391–396.

Borovička J. and Kalenda P. 2003. The Morávka meteorite fall: 4. Meteoroid dynamics and fragmentation in the atmosphere. *Meteoritics & Planetary Science* 38:1023–1043.

Borovička J., Spurný P., and Keclikova J. 1995. A new positional astrometric method for all-sky cameras. *Astronomy & Astrophysics* 112:173.

Borovička J., Spurný P., Kalenda P., and Tagliaferri E. 2003. The Morávka meteorite fall: 1. Description of the events and determination of the fireball trajectory and orbit from video records. *Meteoritics & Planetary Science* 38:975–987.

Bottke W. F., Morbidelli A., Jedicke R., Petit J., Levison H. F., Michel P., and Metcalfe T. S. 2002. Debiased orbital and absolute magnitude distribution of the near-Earth objects. *Icarus* 156:399–433.

Brown P. G. and Edwards W. N. E. 2009. Development of a meteor infrasound observatory. *Inframatics* 23:1–9.

Brown P., Ceplecha Z., Hawkes R., Wetherill G., Beech M., and Mossman K. 1994. The orbit and atmospheric trajectory of the Peekskill meteorite from video records. *Nature* 367:624–626.

Brown P., Hildebrand A., Green D., Page D., Jacobs C., ReVelle D., Tagliaferri E., Wacker J., and Wetmiller B. 1996. The fall of the St-Robert meteorite. *Meteoritics* 31:502–517.

Brown P., Pack D., Edwards W. N., ReVelle D., Yoo B. B., Spalding R. E., and Tagliaferri E. 2004. The orbit, atmospheric dynamics, and initial mass of the Park Forest meteorite. *Meteoritics & Planetary Science* 39:1781–1796.

Brown P., Weryk R. J., Wong D. K., and Jones J. 2008. A meteoroid stream survey using the Canadian Meteor Orbit Radar. I. Methodology and radiant catalogue. *Icarus* 195:317–339.

Brown P., Weryk R. J., Kohut S., Edwards W. N., and Krzeminski Z. 2010. Development of an all-sky video Meteor Network in Southern Ontario, Canada: The ASGARD system. *Journal of the International Meteor Organization* 38:18–23.

Cansi Y. and Le Pichon A. 2008. Infrasound event detection using the progressive multi-channel correlation algorithm. In *Handbook of signal processing in acoustics* edited by Havelock D., Kuwano S., and Vorlander M., chapter 77. New York: Springer. pp. 1425–1435.

Carter R., Jandir P., and Kress M. 2009. Estimating the drag coefficients of meteorites for all Mach number regimes (abstract). 40th Lunar and Planetary Science Conference. p. 2059.

Cartwright J. A., Hermann S., McCausland P. J. A., Brown P., and Ott U. 2010. Noble gas analysis of the Grimsby H chondrite (abstract). 73rd Meeting of the Meteoritical Society. p. A30.

Ceplecha Z. 1961. Multiple fall of Příbram meteorites photographed. 1. Double-station photographs of the fireball and their relations to the found meteorites. *Bulletin of the Astronomical Institute of Czechoslovakia* 12:21–47.

Ceplecha Z. 1977. Fireballs photographed in Central Europe. *Bulletin of the Astronomical Institute of Czechoslovakia* 28:328–340.

Ceplecha Z. 1987. Geometric, dynamic, orbital and photometric data on meteoroids from photographic fireball networks. *Bulletin of the Astronomical Institute of Czechoslovakia* 38:222–234.

Ceplecha Z. 1996. Luminous efficiency based on photographic observations of the Lost City fireball and implications for the influx of interplanetary bodies onto Earth. *Astronomy & Astrophysics* 311:329–332.

Ceplecha Z. and McCrosky R. E. 1976. Fireball end heights: A diagnostic for the structure of meteoric material. *Journal of Geophysical Research* 81:6257–6275.

Ceplecha Z., Spurný P., Borovička J., and Keclicková J. 1993. Atmospheric fragmentation of meteoroids. *Astronomy & Astrophysics* 279:615–626.

Ceplecha Z., Borovička J., Elford W., ReVelle D., Hawkes R. L., Poruban V., and Simek M. 1998. Meteor phenomena and bodies. *Space Science Reviews* 84:327–471.

Chapman C. R. 2004. Space weathering of asteroid surfaces. *Annual Review of Earth and Planetary Sciences* 32:539–567.

Christie D. 2010. The IMS infrasound network: Design and establishment of infrasound stations. In *Infrasound monitoring for atmospheric studies*, edited by Le Pichon A., Blanc E., and Hauchecorne A. Dordrecht: Springer. pp. 27–72.

Close S., Oppenheim M., Hunt S., and Coster A. 2004. A technique for calculating meteor plasma density and meteoroid mass from radar head echo scattering. *Icarus* 168:43–52.

Consolmagno G. J. and Drake M. J. 1977. Composition and evolution of the eucrite parent body: Evidence from rare earth elements. *Geochimica et Cosmochimica Acta* 41:1271–1282.

Crum T. and Alberty R. 1993. The WSR-88D and the WSR-88D Operational Support Facility. *Bulletin of the American Meteorological Society* 74:1669–1687.

Dyrud L., Wilson D., Boerve S., Trulsen J., Pecseli H., Close S., Chen C., and Lee Y. 2008. Plasma and electromagnetic simulations of meteor head echo radar reflections. *Earth, Moon, and Planets* 102:383–394.

Dziewonski A. and Hales A. 1972. *Methods in computational physics*, vol. 11. New York: Academic Press. pp. 39–84.

Edwards W. N. and Hildebrand A. R. 2004. SUPRACENTER: Locating fireball terminal bursts in the atmosphere using seismic arrivals. *Meteoritics & Planetary Science* 39:1449–1460.

Edwards W. N., Brown P. G., and ReVelle D. O. 2006. Estimates of meteoroid kinetic energies from observations of infrasonic airwaves. *Journal of Atmospheric and Solar-Terrestrial Physics* 68:1136–1160.

Edwards W. N., Brown P. G., Weryk R. J., and ReVelle D. O. 2007. Infrasonic observations of meteoroids: Preliminary results from a coordinated optical-radar-infrasound observing campaign. *Earth, Moon, and Planets* 102:221–229.

Evers L. G. and Haak H. W. 2003. Tracing a meteoric trajectory with infrasound. *Geophysical Research Letters* 30, doi:10.1029/2003GL017947.

Fries M. and Fries J. 2010. Partly cloudy with a chance of chondrites—Studying meteorite falls using Doppler weather radar (abstract). 41st Lunar and Planetary Science Conference. p. 1179.

Goswami J., Lal D., Rao M., Sinha N., and Venkatesan T. 1978. Particle track and rare gas studies of Innisfree meteorite (abstract). *Meteoritics*. pp. 481–484.

Halliday I., Blackwell A., and Griffin A. 1978. The Innisfree meteorite and the Canadian camera network. *Journal of the Royal Astronomical Society of Canada* 72:15–39.

Halliday I., Griffin A. A., and Blackwell A. T. 1981. The Innisfree meteorite fall: A photographic analysis of

fragmentation, dynamics and luminosity. *Meteoritics* 16: 153–170.

Hildebrand A., McCausland P. J., Brown P., Longstaffe F. J., Russell S. D., Tagliaferri E., Wacker J., and Mazur M. J. 2006. The fall and recovery of the Tagish Lake meteorite. *Meteoritics & Planetary Science* 41:407–431.

Jenniskens P., Shaddad M. H., Numan D., Elsir S., Kudoda A. M., Zolensky M. E., Le L., Robinson G. A., Friedrich J. M., Rumble D., Steele A., Chesley S. R., Fitzsimmons A., Duddy S., Hsieh H. H., Ramsay G., Brown P. G., Edwards W. N., Tagliaferr E., Boslough M. B., Spalding R. E., Dantowitz R., Kozubal M., Pravec P., Borovička J., Charvat Z., Vaubaillon J., Kuiper J., Albers J., Bishop J. L., Mancinelli R. L., Sandford S.A., Milam S. N., Nuevo M., and Worden S. P. 2009. The impact and recovery of asteroid 2008 TC_3. *Nature* 458:485–488.

Jones J., Webster A. R., and Hocking W. K. 1998. An improved interferometer design for use with meteor radars. *Radio Science* 33:55–65.

Jones J., Brown P., Ellis K. J., Webster A. R., Campbell-Brown M., Krzemenski Z., and Weryk R. J. 2005. The Canadian Meteor Orbit Radar: System overview and preliminary results. *Planetary and Space Science* 53:413–421.

Keay C. 1992. Electrophonic sounds from large meteor fireballs. *Meteoritics* 27:144–148.

Lemon L. 1999. WSR-88D/98D: Operational capabilities and applications, weather and biological targets. Proceedings, International Seminar on Birds and Flight Safety in the Middle East, Israel, April 25–29. pp. 261–281.

McCausland P., Brown P., Hildebrand A., Flemming R., Barker I., Moser D., Renaud J., and Edwards W. 2010. Fall of the Grimsby H5 chondrite (abstract). 41st Lunar and Planetary Science Conference. p. 2716.

McCrosky R., Posen A., Schwartz G., and Shao C. 1971. Lost City meteorites: Its recovery and a comparison with other fireballs. *Journal of Geophysical Research* 76:4090–4108.

Milley E. P., Hildebrand A., Brown P., Noble M., Sarty G., Ling A., and Mailler L. 2010. Pre-fall orbit of the Buzzard Coulee meteoroid. Presented at Geocanada 2010, Calgary, Alberta, May 10–14, 2010.

Popova O. P., Hartmann W. K., Borovička J., Spurný P., Trigo-Rodríguez J., Gnos E., and Nemtchinov I. Forthcoming. Very low strengths of interplanetary meteoroids and small asteroids. *Meteoritics & Planetary Science*.

ReVelle D. O. 1974. *Acoustics of meteors—Effects of the atmospheric temperature and wind structure on the sounds produced by meteors*. Ph.D. dissertation, University of Michigan, Ann Arbor, Michigan.

ReVelle D. O. 1976. On meteor-generated infrasound. *Journal of Geophysical Research* 81:1217–1229.

ReVelle D. and Rajan R. 1979. On the luminous efficiency of meteoritic fireballs. *Journal of Geophysical Research* 84:6255–6262.

Skolnik M. 2001. *Introduction to radar systems*, 3rd ed. New York: McGraw-Hill. 748 p.

Spurný P., Oberst J., and Heinlein D. 2003. Photographic observations of Neuschwanstein, a second meteorite from the orbit of the Příbram chondrite. *Nature* 423:151–153.

Spurný P., Borovička J., Kac J., Kalenda P., Atanackov J., Kladnik G., Heinlein D., and Grau T. 2010. Analysis of instrumental observations of the Jesenice meteorite fall on April 9, 2009. *Meteoritics & Planetary Science* 45:1392–1407.

Swinbank R. and O'Neill A. A. 1994. Stratosphere–troposphere data assimilation system. *Monthly Weather Review* 122:686–702.

Taylor A. D., Cervera M. A., Elford W. G., and Steel D. I. 1996. A new technique for radar meteor speed determination: Inter-pulse phase changes from head echoes. In *Physics, chemistry and dynamics of interplanetary dust*, edited by Gustafson B. A. S. and Hanner M. S.. Proceedings of the 150th colloquium of the International Astronomical Union, Gainsville, FL, August 14–18, 1995. 75 p.

Trigo-Rodríguez J., Borovička J., Spurný P., Ortiz J. L., Docobo J. A., Castro-Tirado A. J., and Llorca J. 2006. The Villalbeto de la Peña meteorite fall: II. Determination of atmospheric trajectory and orbit. *Meteoritics & Planetary Science* 41:505–517.

Veres P., Jedicke R., Wainscoat R., Granvik M., Chesley S., Abe S., Denneau L., and Grav T. 2009. Detection of Earth-impacting asteroids with the next generation all-sky surveys. *Icarus* 203:472–485.

Weryk R. J., Brown P. G., Domokos A., Edwards W. N., Krzeminski Z., Nudds S. H., and Welch D. L. 2007. The Southern Ontario all-sky meteor camera network. *Earth, Moon, and Planets* 102:241–246.

Wetherill G. and ReVelle D. 1981. Which fireballs are meteorites? A study of the Prairie Network photographic meteor data. *Icarus* 48:308–328.

Yano H., Kubota T., Miyamoto H., Okada T., Scheeres D., Takagi Y., Yoshida K., Abe M., Abe S., Barnouin-Jha O., Fujiwara A., Hasegawa S., Hashimoto T., Ishiguro M., Kato M., Kawaguchi J., Mukai T., Saito J., Sasaki S., and Yoshikawa M. 2006. Touchdown of the Hayabusa spacecraft at the Muses Sea on Itokawa. *Science* 312:1350–1353.

Young C. J., Chael E. P., and Merchant B. J. 2002. Version 1.7 of MatSeis and the GNEM R&E regional seismic analysis tools. Proceedings, 24th Seismic Research Review. pp. 915–924. CD-ROM.